

How Stationary Eddies Shape Changes in the Hydrological Cycle: Zonally Asymmetric Experiments in an Idealized GCM

ROBERT C. WILLS AND TAPIO SCHNEIDER

California Institute of Technology, Pasadena, California, and ETH Zürich, Zurich, Switzerland

(Manuscript received 31 October 2015, in final form 9 February 2016)

ABSTRACT

Stationary and low-frequency Rossby waves are the primary drivers of extratropical weather variations on monthly and longer time scales. They take the form of persistent highs and lows, which, for example, shape subtropical dry zones and guide extratropical storms. More generally, stationary-eddy circulations, including zonally anomalous tropical overturning circulations, set up large zonal variations in net precipitation (precipitation minus evaporation, $P - E$). This paper investigates the response of stationary eddies and the zonally asymmetric hydrological cycle to global warming in an idealized GCM, simulating a wide range of climates by varying longwave absorption. The stationary eddies are forced by two idealized zonal asymmetries: a midlatitude Gaussian mountain and an equatorial ocean heat source. Associated with changes in stationary eddies are changes in the zonal variation of the hydrological cycle. Particularly in the subtropics, these simulations show a nearly constant or decreasing amplitude of the zonally anomalous hydrological cycle in climates warmer than modern despite the *wet gets wetter, dry gets drier* effect associated with increasing atmospheric moisture content. An approximation for zonally anomalous $P - E$, based on zonal-mean surface specific humidity and stationary-eddy vertical motion, disentangles the roles of thermodynamic and dynamic changes. The approximation shows that changes in the zonally asymmetric hydrological cycle are predominantly controlled by changes in lower-tropospheric vertical motion in stationary eddies.

1. Introduction

The tendency for wet latitude bands to get wetter and for dry latitude bands to get drier has been highlighted as a robust response of the zonal-mean hydrological cycle to global warming (Mitchell et al. 1987; Chou and Neelin 2004; Held and Soden 2006). As Held and Soden (2006) point out, this *wet gets wetter, dry gets drier* response relies on the assumption of fixed relative humidity and circulation. These assumptions are expected to break down for variations about the zonal mean due to land–sea differences in relative humidity and moisture gradient changes (Byrne and O’Gorman 2013, 2015; Greve et al. 2014) and due to changes in stationary-eddy circulations, which we will explore in this paper.

In the extratropics, large-scale stationary-eddy circulations take the form of Rossby waves. Stationary and low-frequency Rossby waves contribute to the maintenance of midlatitude and subtropical dry zones (Broccoli and Manabe 1992; Rodwell and Hoskins 1996, 2001;

Takahashi and Battisti 2007) and monsoonal wet zones (Molnar et al. 2010; Chen and Bordoni 2014). Changes in stationary Rossby waves with climate change could thus have large regional impacts on the hydrological cycle. Such changes have already been implicated in the increasing aridification of southwest North America and the Mediterranean region (Seager et al. 2007, 2014a,b).

In the tropics, stationary-eddy (i.e., zonally anomalous) overturning circulations such as Walker circulations have a profound influence on the spatial pattern of tropical precipitation and exhibit variability on interannual time scales, for example, associated with the El Niño–Southern Oscillation (ENSO). The reduction of overturning in these circulations has been highlighted as a robust response to global warming, with a profound influence on the zonally anomalous hydrological cycle (Held and Soden 2006; Vecchi and Soden 2007; Chadwick et al. 2013). Tropical overturning circulations and the associated wet zones can also shift with warming according to the *warm gets wetter* mechanism (Xie

Corresponding author address: Robert C. Wills, Geological Institute, ETH Zurich, Sonneggstrasse 5, 8092 Zurich, Switzerland.
E-mail: robert.wills@erdw.ethz.ch

Publisher’s Note: This article was revised on 22 April 2016 to fix a production error that degraded the quality of Figs. 2, 3, 4, 6, 7, 8, 9, and 11, and to correct typesetting errors for variables containing an overbar and asterisk.

et al. 2010), where convection shifts to regions with amplified warming. Both of these mechanisms can limit the utility of the *wet gets wetter, dry gets drier* mechanism through changes in stationary-eddy overturning.

Several studies have analyzed changes in stationary-eddy streamfunction (Stephenson and Held 1993; Brandefelt and Körnich 2008; Simpson et al. 2014, 2016) and tropical convective mass flux (Knutson and Manabe 1995; Vecchi and Soden 2007; Ma et al. 2012) with global warming. While these studies of comprehensive climate change scenarios yield insight into how stationary eddies may change with warming in the real climate system, multiple stationary-eddy sources make it difficult to ascertain the mechanisms for the simulated changes. With this in mind, we design two idealized GCM experiments in which simple zonal asymmetries are added to an aquaplanet. We analyze changes in stationary eddies and the associated changes in the hydrological cycle in these experiments.

In section 2, we describe two idealized GCM experiments with zonally asymmetric boundary conditions. In section 3, we compare the simulated net precipitation [precipitation minus evaporation ($P - E$)] changes to expectations from the *wet gets wetter, dry gets drier* mechanism, revealing the importance of changes in atmospheric circulations. In section 4, we analyze the zonally anomalous moisture and vorticity budgets to gain insight into the circulations responsible for zonal variation of $P - E$ in these experiments. In section 5, we analyze changes in zonally anomalous $P - E$ using the moisture-budget balance developed in section 4. The result is that changes in zonally anomalous $P - E$ can be understood in terms of changes in lower-tropospheric vertical motion in stationary eddies, which we discuss in section 6. Conclusions are given in section 7.

2. Zonally asymmetric aquaplanet experiments

Stationary eddies are primarily forced by topography and zonally anomalous surface heating (Hoskins and Karoly 1981; Held et al. 2002). We set up two sets of aquaplanet simulations to study these forcings separately in an idealized setting. The forcing of stationary eddies by zonal anomalies of transient-eddy heat fluxes and diabatic heating are often considered separately (e.g., Held et al. 2002). Here the model computes all zonally anomalous heating internal to the atmosphere explicitly; hence, this heating evolves with climate change. In this way, we consider the total stationary-wave response to zonally anomalous external forcing.

a. Model

We use an idealized GCM based on the GFDL Flexible Modeling System (<http://www.gfdl.noaa.gov/fms>).

The convection scheme is essentially that of Frierson et al. (2006) and Frierson (2007), with the modifications described in O’Gorman and Schneider (2008). The model has a horizontal spectral resolution of T85. Our model setup is similar to O’Gorman and Schneider (2008) except that we have extended the vertical domain up to $\sigma = p/p_s = 4 \times 10^{-4}$ (pressure p and surface pressure p_s) with 38 vertical levels and have included linear damping in an 8-level sponge layer at the top of the domain. The linear damping coefficient increases linearly by level from $14\,400\text{ s}^{-1}$ at the lowest sponge level to 1800 s^{-1} at the top model level and is applied only to anomalies from the zonal mean. This helps minimize reflections of stationary waves from the top of the domain.¹

All experiments are run in a perpetual equinox setup, avoiding complexity associated with the seasonal cycle. Radiative transfer is represented by a two-stream scheme for a semigray atmosphere, meaning that there are no water vapor or cloud radiative feedbacks. Water vapor and cloud radiative feedbacks have been shown to influence the circulation response to global warming in climate models (e.g., Voigt and Shaw 2015). However, we focus on understanding the simple case presented here without these feedbacks, as it is an important prerequisite to a complete understanding. In the gray atmosphere, climate change can be simulated by varying the longwave optical depth, $\tau = \alpha\tau_{\text{ref}}$, where τ_{ref} is a reference optical depth that varies as a function of latitude ϕ and normalized pressure σ ,

$$\tau_{\text{ref}}(\phi, \sigma) = [f_l\sigma + (1 - f_l)\sigma^4][\tau_e + (\tau_p - \tau_e)\sin^2\phi], \quad (1)$$

and α is a multiplicative factor. Here $f_l = 0.2$, and the longwave optical thickness at the equator and pole are $\tau_e = 7.2$ and $\tau_p = 1.8$, respectively. To simulate climates with global-mean surface temperatures ranging from 280 to 316 K, we use $\alpha = [0.6, 0.7, 0.8, 0.9, 1.0, 1.2, 1.4, 1.6, 1.8, 2.0, 2.5, 3.0, 4.0, 6.0]$. We refer to $\alpha = 1.0$ as the reference climate, which has a global-mean surface temperature of 289 K. Each simulation is spun up for at least 4 years. All fields shown are averages over the subsequent 8 years.

The surface boundary condition is a 1-m slab ocean with its own surface energy balance, such that surface energy fluxes are freely evolving. Surface fluxes of momentum, latent heat, and sensible heat are computed using Monin–Obukhov similarity theory, with a roughness

¹ One simulation, the coldest equatorial heating simulation, is run with double the sponge-layer damping coefficients to avoid numerical instabilities in the stratosphere.

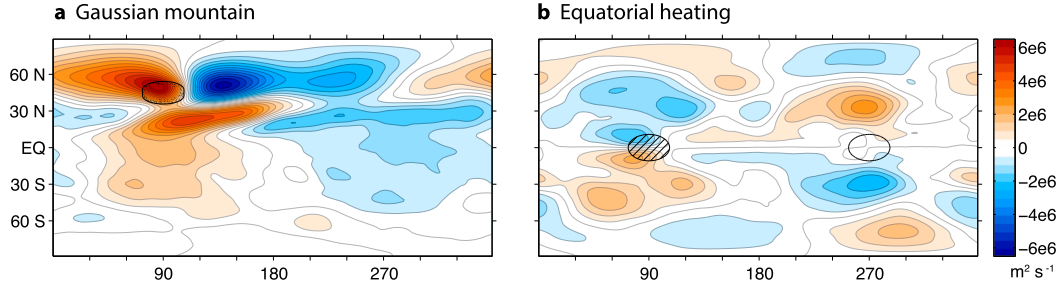


FIG. 1. Experimental setup and stationary-eddy streamfunction at $p = 600$ hPa in the reference climate ($\alpha = 1$) of (a) the Gaussian mountain experiment and (b) the equatorial heating experiment. The black contour in (a) is the 1000-m contour of surface height. In (b), the black circles are the $\pm 20 \text{ W m}^{-2}$ contours of zonally anomalous ocean heat-flux divergence, $\nabla \cdot \mathbf{F}_1$. The hashed circle is the location of the heating (ocean heat-flux convergence). The same reference contours are shown in all subsequent map plots.

length of 5×10^{-3} m for momentum and 1×10^{-5} m for latent and sensible heat, as in O’Gorman and Schneider (2008). To simulate a more realistic zonal-mean climate in the tropics, we add a zonal-mean ocean heat-flux convergence:

$$\nabla \cdot \mathbf{F}_0(\phi) = Q_0 \left(1 - 2 \frac{\phi^2}{\phi_0^2} \right) \exp \left(-\frac{\phi^2}{\phi_0^2} \right). \quad (2)$$

As in Bordoni (2007), Bordoni and Schneider (2008), and Merlis and Schneider (2011), we choose values that give an ocean heat-flux convergence similar to the hemispherically and zonally symmetric component in observations: $Q_0 = 50 \text{ W m}^{-2}$ and $\phi_0 = 16^\circ$.

b. Gaussian mountain range

To study the response of orographically forced stationary waves and the associated wet and dry zones to warming in this idealized model, we add a single Gaussian mountain ridge in midlatitudes. The surface height as a function of longitude λ and latitude ϕ is given by

$$z_{\text{stc}}(\lambda, \phi) = h_0 \exp \left[-\frac{(\lambda - \lambda_0)^2}{2\sigma_\lambda^2} - \frac{\max(0, |\phi - \phi_0| - R_\phi)^2}{2\sigma_\phi^2} \right]. \quad (3)$$

We use $h_0 = 2500$ m, $\phi_0 = 45^\circ\text{N}$, $R_\phi = 2.5^\circ$, $\sigma_\phi = 5^\circ$, and $\sigma_\lambda = 12.5^\circ$. As there are no other zonal asymmetries, λ_0 is arbitrary. It will be denoted 90° on plots. The latitudinal position and size of this mountain range are such that it is comparable to the Rocky Mountains. The amplitude of Rossby waves forced is sensitive to the choice of σ_λ and h_0 . We choose these values to maximize the Rossby wave response while keeping the mountain size realistic.

No modifications are made to the surface properties; thus, this mountain is an aquamountain. Modified simulations with a bucket model for surface hydrology and/or a modified surface heat capacity in the vicinity of the mountain do not have a large influence on the large-scale balances described here.

Figure 1a shows the 600-hPa stationary-eddy streamfunction response to the mountain. There is both poleward and equatorward deflection of the flow around the mountain. This leads to wave trains propagating poleward and equatorward, with the eastward group velocity characteristic of Rossby waves. The equatorward Rossby wave train has a large influence on the moisture budget all the way to the equator (Fig. 2). In Fig. 1a and all subsequent figures, the 1000-m contour of surface height is shown with a black contour, with speckling on the upslope side.

c. Tropical ocean heat transport

To study the response of stationary eddies forced by tropical heating to warming in this idealized configuration, we add ocean heating and cooling along the equator. The experimental setup is similar to that of Merlis and Schneider (2011), where the zonal symmetry is broken by adding an ocean heat-flux divergence:

$$\nabla \cdot \mathbf{F}_1(\lambda, \phi) = Q_1 \exp \left[-\frac{(\lambda - \lambda_E)^2}{2\sigma_\lambda^2} - \frac{\phi^2}{2\sigma_\phi^2} \right] - Q_1 \exp \left[-\frac{(\lambda - \lambda_W)^2}{2\sigma_\lambda^2} - \frac{\phi^2}{2\sigma_\phi^2} \right]. \quad (4)$$

We use $Q_1 = 50 \text{ W m}^{-2}$, $\lambda_W = 90^\circ$, $\lambda_E = 270^\circ$, $\sigma_\lambda = 12.5^\circ$, and $\sigma_\phi = 8^\circ$.

This setup drives a Walker circulation with ascending branch at 90° longitude and descending branch at 270° . The large-scale divergence/convergence generates

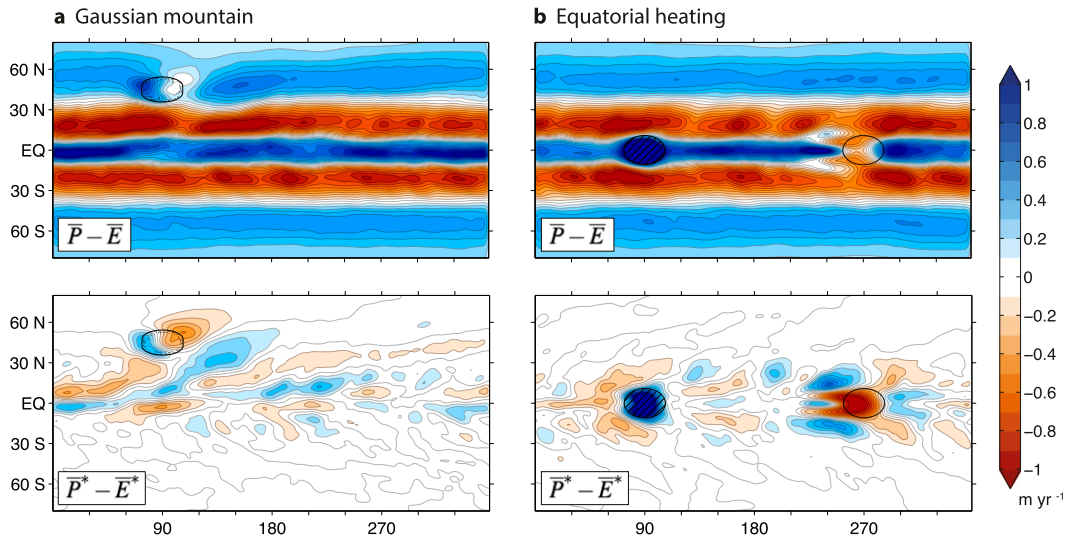


FIG. 2. $\bar{P} - \bar{E}$ and $\bar{P}^* - \bar{E}^*$ in the reference climate ($\alpha = 1$) of (a) the Gaussian mountain experiment and (b) the equatorial heating experiment. Here and in all subsequent latitude–longitude figures, the fields are smoothed with a 1.5° real-space Gaussian filter to focus on large scales. This makes very little difference here, but gets rid of distracting grid-scale noise due to differentiation in later figures. Note that values of $\bar{P} - \bar{E}$ ($\bar{P}^* - \bar{E}^*$) are up to 2.5 (1.6) m yr^{-1} over the equatorial heating, where we allow the color map to saturate to focus also on subtropical $\bar{P} - \bar{E}$ patterns. (See Fig. 1 text for reference contour information.).

rotational flow and hence Rossby waves, which propagate into the extratropics (Sardeshmukh and Hoskins 1988). The stationary-eddy streamfunction at 600 hPa is shown in Fig. 1b, as well as the locations of the heating (hatched circle) and cooling (open circle). The region of equatorial heating gives rise to lower-tropospheric cyclonic circulations in both hemispheres and anticyclones aloft. The region of equatorial cooling gives rise to the opposite directionality of circulations.

3. The zonally anomalous hydrological cycle

Idealized GCM experiments have been used to understand the physical balances of the zonal-mean hydrological cycle (e.g., O’Gorman and Schneider 2008). The zonally asymmetric experiments presented here allow us to analyze the physical mechanisms of the departures from the zonal-mean hydrological cycle. We focus in particular on understanding the mechanisms behind zonal anomalies in net precipitation, $\bar{P}^* - \bar{E}^*$ (i.e., the zonally anomalous atmospheric hydrological cycle). Here $(\bar{\cdot})$ represents a long-term time mean and $(\bar{\cdot})^*$ represents a departure from a zonal mean $[\cdot]$, such that the full field can be written as $(\bar{\cdot}) = [\cdot] + (\bar{\cdot})^*$. Figure 2 shows the full time-mean net precipitation $\bar{P} - \bar{E}$ as well as the stationary-eddy component $\bar{P}^* - \bar{E}^*$ in the reference climate of each experiment. The stationary-eddy component is dominated by the zonal variation of precipitation, \bar{P}^* . The zonal variation of evaporation is

only important directly over the topography or the ocean heating/cooling region.

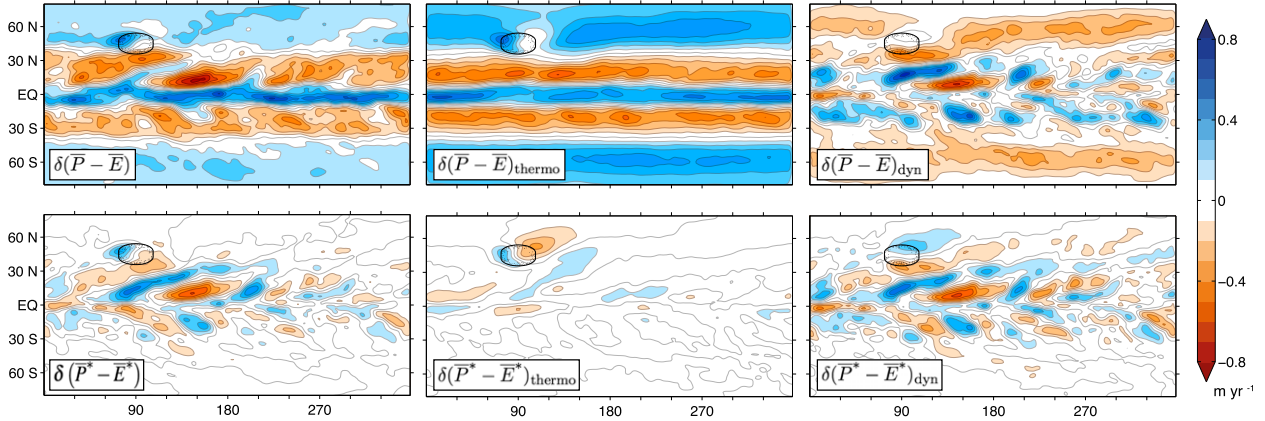
The Gaussian mountain leads to a wet zone of orographic precipitation upstream of the mountain range, a large dry zone extending poleward and more than 30° downstream, and an alternating pattern of wet and dry zones in the subtropics and tropics associated with an equatorward Rossby wave train (Fig. 2a). Some influence of this Rossby wave train is also seen in the Southern Hemisphere subtropics. This equatorward wave train does not show up in experiments with a narrower mountain range (cf. Shi and Durran 2014).

The equatorial heating/cooling leads to an area of localized high $\bar{P} - \bar{E}$ over the ocean heat-flux convergence, a large region of dryness immediately to the west, an extended area of low $\bar{P} - \bar{E}$ around the ocean heat-flux divergence, and large wet zones immediately west and poleward (Fig. 2b). We would like to understand the physics maintaining these regional $\bar{P} - \bar{E}$ differences and look at how the patterns respond to climate change.

a. Response to climate change

First, we would like to discuss some basic expectations of how $\bar{P} - \bar{E}$ and, in particular, its stationary-eddy component $\bar{P}^* - \bar{E}^*$ should respond to climate change. In the absence of changes in atmospheric circulations or the spatial structure of specific humidity, $\bar{P} - \bar{E}$ would change thermodynamically, following the change in surface specific humidity \bar{q}_{sfc} (cf. Held and Soden 2006):

a Gaussian mountain



b Equatorial heating

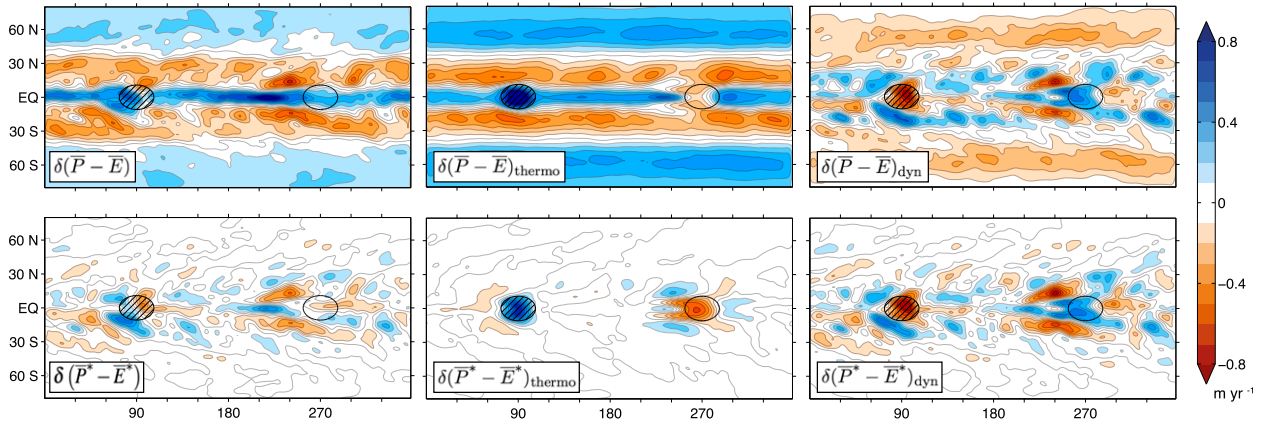


FIG. 3. Change in total $\bar{P} - \bar{E}$, $\delta(\bar{P} - \bar{E})$, and in $\bar{P}^* - \bar{E}^*$, $\delta(\bar{P}^* - \bar{E}^*)$, from the reference climate ($\alpha = 1$) to the climate with 1.4 times the optical depth ($\alpha = 1.4$), corresponding to a 4.7-K increase in global-mean surface temperature. (a) Gaussian mountain experiment. (b) Equatorial heating experiment. The changes are split into a thermodynamic component, based on the fractional change of surface specific humidity, and a residual “dynamic” component, showing all other types of change. (See Fig. 1 text for reference contour information.)

$$\delta(\bar{P} - \bar{E})_{\text{thermo}} \approx \frac{\delta \bar{q}_{\text{sfic}}}{(\bar{q}_{\text{sfic}})_0} (\bar{P}_0 - \bar{E}_0), \quad (5)$$

where $\delta(\cdot) = (\cdot) - (\cdot)_0$ is the change of a quantity from the reference simulation. Quantities in the reference simulation are denoted by $(\cdot)_0$. The increase in saturation specific humidity with warming means that wet zones get wetter and dry zones get drier, with a rate determined by the Clausius–Clapeyron (C–C) relation, up to possible changes in near-surface relative humidity, which are generally small (Held and Soden 2000, 2006; Schneider et al. 2010). This *wet gets wetter, dry gets drier* scaling is qualitatively a good approximation for $\delta(\bar{P} - \bar{E})$ in the zonal mean and ocean-basin zonal mean (Held and Soden 2006; Byrne and O’Gorman 2015). Byrne and O’Gorman (2015) show how moisture gradient changes can affect $\delta(\bar{P} - \bar{E})$ in a purely thermodynamic way, especially over land. We will show how

changes in atmospheric circulations affect $\delta(\bar{P} - \bar{E})$ and limit the utility of this simple thermodynamic relationship regionally.

While this *wet gets wetter, dry gets drier* scaling is often quoted in reference to regional $\bar{P} - \bar{E}$ changes, there has been little analysis of the extent to which this actually applies. Several studies have even shown that, because of the lack of angular momentum constraints on zonal circulations, any weakening of the hydrological cycle required by energetic constraints may preferentially be taken up by zonal anomalies (Held and Soden 2006; Vecchi and Soden 2007; Schneider et al. 2010; Merlis and Schneider 2011). We might therefore expect that the *wet gets wetter, dry gets drier* scaling does not apply well for zonal anomalies because of changes in stationary-eddy circulations.

A comparison of $\delta(\bar{P} - \bar{E})$ and $\delta(\bar{P} - \bar{E})_{\text{thermo}}$ is shown in Fig. 3 for changes between the reference simulation ($\alpha = 1$) and a simulation with 40% greater optical depth

($\alpha = 1.4$). The simple thermodynamic scaling captures the sign of changes in most places but generally overestimates the magnitude of changes. The residual “dynamic” change, $\delta(\bar{P} - \bar{E})_{\text{dyn}} = \delta(\bar{P} - \bar{E}) - \delta(\bar{P} - \bar{E})_{\text{thermo}}$, shows a slowdown of the hydrological cycle, especially in the storm tracks. The conclusions are qualitatively similar for 10% and 20% increases in optical depth or for a 10% decrease in optical depth.

The stationary-eddy components of these changes are shown below the full fields in Fig. 3. The thermodynamic component of the stationary-eddy change,

$$\delta(\bar{P}^* - \bar{E}^*)_{\text{thermo}} \approx \frac{\delta[\bar{q}_{\text{sfc}}]}{[\bar{q}_{\text{sfc}}]_0} (\bar{P}_0^* - \bar{E}_0^*), \quad (6)$$

is much smaller than the simulated changes and does not generally capture the sign of changes.² This suggests that because stationary-eddy circulations are freer to change in magnitude and location in response to climate change than zonal-mean circulations, the *wet gets wetter, dry gets drier* paradigm is not useful for anomalies from the zonal mean. While there are several other ways in which one can split $P - E$ changes into thermodynamic and dynamic components (Wu et al. 2011; Seager et al. 2010; Bony et al. 2013; Byrne and O’Gorman 2015), none of them change this conclusion: changes in stationary-eddy circulations are of first-order importance for $\delta(\bar{P}^* - \bar{E}^*)$ in these experiments.

Stationary-eddy changes in the Gaussian mountain experiment take the form of a phase shift of the equatorward Rossby wave train, as can be seen from the different phasing of subtropical wet and dry zones between $\delta(\bar{P}^* - \bar{E}^*)_{\text{thermo}}$ and $\delta(\bar{P}^* - \bar{E}^*)$ in Fig. 3. This results from differences in the meridional group propagation of stationary Rossby waves in a climate with a different zonal-mean circulation (Hoskins and Karoly 1981).

In the equatorial heating experiment, it can be seen from Fig. 3 that $\delta(\bar{P}^* - \bar{E}^*)_{\text{thermo}}$ is opposite in sign to $\delta(\bar{P}^* - \bar{E}^*)$ in most locations. The dynamic change gives evidence of shifting locations of ascent and descent, as well as a general weakening of tropical overturning. The change in strength of overturning will become clearer as we examine the zonal variance of $\bar{P}^* - \bar{E}^*$.

b. Changes in zonal variance of net precipitation

Since the geometry of these experiments is idealized and no region in the model corresponds exactly to a

region in the real world, it is helpful to analyze the variance of $\bar{P}^* - \bar{E}^*$ averaged over a large region, such as a latitude band. While the particular change of stationary-wave phase structure in these experiments would be difficult to generalize to the real world, the change in strength of stationary-eddy circulations may be more general. Therefore, we analyze the root zonal-mean square $\bar{P}^* - \bar{E}^*$, which we denote by $\text{rms}(\bar{P}^* - \bar{E}^*)$, with

$$\text{rms}(\cdot) \equiv \sqrt{[(\cdot)^2]}. \quad (7)$$

Figure 4 shows the climatology of $\text{rms}(\bar{P}^* - \bar{E}^*)$ in the reference climate of both experiments as well as the change in response to a 40% increase in optical depth.

If these changes were purely thermodynamic, we would expect a fairly uniform percentage increase for all latitude bands following the percentage increase in surface specific humidity, $\delta[\bar{q}_{\text{sfc}}]/[\bar{q}_{\text{sfc}}]_0$, which is shown as a blue line in Fig. 4c. Note that $\delta[\bar{q}_{\text{sfc}}]/[\bar{q}_{\text{sfc}}]_0$ is larger than 7% per kelvin because the temperature difference between these climates is large enough that the linear approximation to C–C does not hold. Relative humidity changes are small, consistent with the arguments of Held and Soden (2000). Latitudinal variations of $\delta[\bar{q}_{\text{sfc}}]/[\bar{q}_{\text{sfc}}]_0$ also arise primarily from the nonlinearity of the C–C relation.

The fractional change of $\text{rms}(\bar{P}^* - \bar{E}^*)$ is not far from the thermodynamic expectation for the Southern Hemisphere of the simulations forced by Northern Hemisphere orography, though the absolute magnitude of $\text{rms}(\bar{P}^* - \bar{E}^*)$ is small because the Southern Hemisphere’s surface is zonally symmetric. Closer to the mountain, where zonal variations are larger, the response is more complex, with some regions near the mountain where the zonal variance of the hydrological cycle increases much less than the thermodynamic expectation (blue line in Figs. 4b and 4c), and regions in the Northern Hemisphere subtropics where it increases much more than the thermodynamic expectation. While the response of $\text{rms}(\bar{P}^* - \bar{E}^*)$ far from the mountain is close to thermodynamic, there appear to be large dynamic changes in the entire hemisphere of the mountain.

The situation for the equatorial heating experiment is similar: changes in $\text{rms}(\bar{P}^* - \bar{E}^*)$ within 30° latitude of the forcing, where $\text{rms}(\bar{P}^* - \bar{E}^*)$ is largest, have a complex spatial structure that must be influenced by changes in the strength of stationary-eddy circulations. Beyond 30° latitude, the change is closer to that expected from the increase in atmospheric moisture content, though at high latitudes, the fractional change is considerably less than the fractional change of surface specific humidity. The most interesting feature is that $\text{rms}(\bar{P}^* - \bar{E}^*)$ actually decreases in the subtropics,

² An alternative definition, which includes changes in zonally anomalous moisture, $\delta(\bar{P}^* - \bar{E}^*)_{\text{thermo}} \approx \{\delta\bar{q}_{\text{sfc}}/\bar{q}_{\text{sfc}0}(\bar{P}_0 - \bar{E}_0)\}^*$, differs by less than 0.1 m yr⁻¹ in all regions. We maintain the $[\bar{q}_{\text{sfc}}]$ definition for the simplicity of its interpretation.

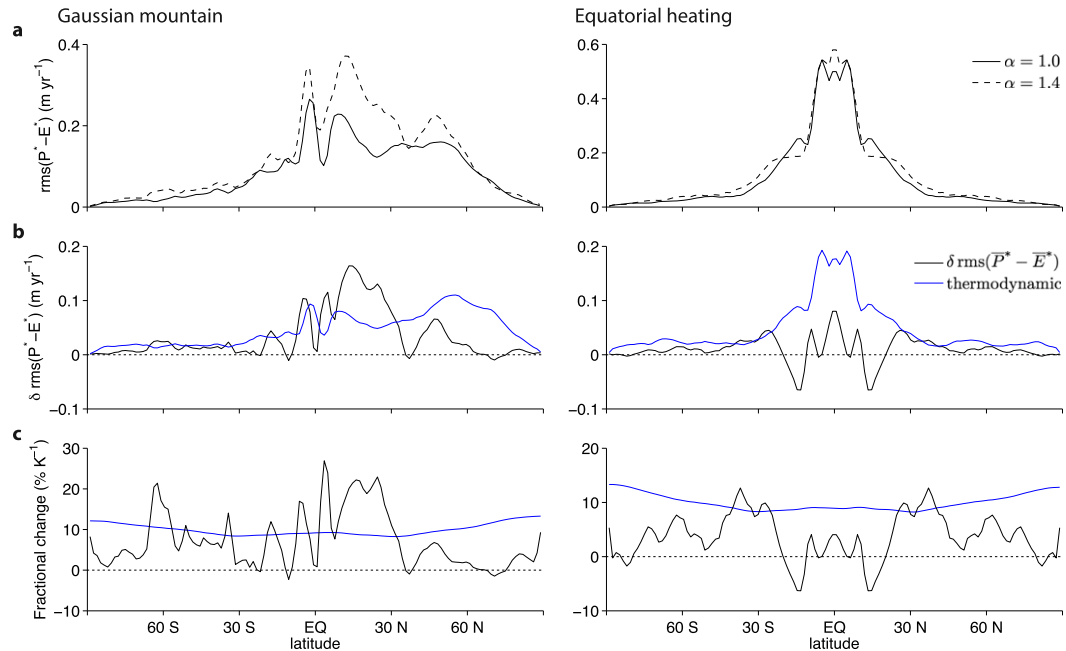


FIG. 4. (a) Climatology of $\text{rms}(\overline{P^*} - \overline{E^*})$ in the simulations with $\alpha = 1.0$ (solid) and $\alpha = 1.4$ (dashed). (b) Change in $\text{rms}(\overline{P^*} - \overline{E^*})$ with global warming between $\alpha = 1.0$ and $\alpha = 1.4$ and its thermodynamic component [rms applied to Eq. (6), blue line]. (c) Fractional change in $\text{rms}(\overline{P^*} - \overline{E^*})$ per degree of zonal-mean warming and its thermodynamic component ($\delta[q_{\text{sfic}}]/[q_{\text{sfic}}]$, blue line). Each plot is shown for (left) the Gaussian mountain experiment and (right) the equatorial heating experiment. Note that values have been symmetrized about the equator for the equatorial heating experiment.

meaning that even for a bulk quantity like $\text{rms}(\overline{P^*} - \overline{E^*})$, dynamic changes can be strong enough to reverse the tendency toward *wet gets wetter, dry gets drier*. The complexity of $\text{rms}(\overline{P^*} - \overline{E^*})$ continues throughout the range of climates, as shown in Fig. 5, which would scale up exponentially from left to right if it were not for dynamic changes.

To understand the mechanisms governing the apparent dynamic changes in $\overline{P^*} - \overline{E^*}$ and $\text{rms}(\overline{P^*} - \overline{E^*})$, we must first understand which circulations are responsible for the zonal variation of net precipitation. Toward this end, we proceed to decompose the zonally anomalous

moisture and vorticity budgets in these experiments following Wills and Schneider (2015, hereafter WS15).

4. Physical balances

a. Moisture budget decomposition

WS15 outline a decomposition of the zonally anomalous moisture budget to understand $\overline{P^*} - \overline{E^*}$ in ERA-Interim reanalysis. Here, we proceed in a similar fashion to understand which types of circulations are important for maintaining zonal variation of $\overline{P} - \overline{E}$ in these

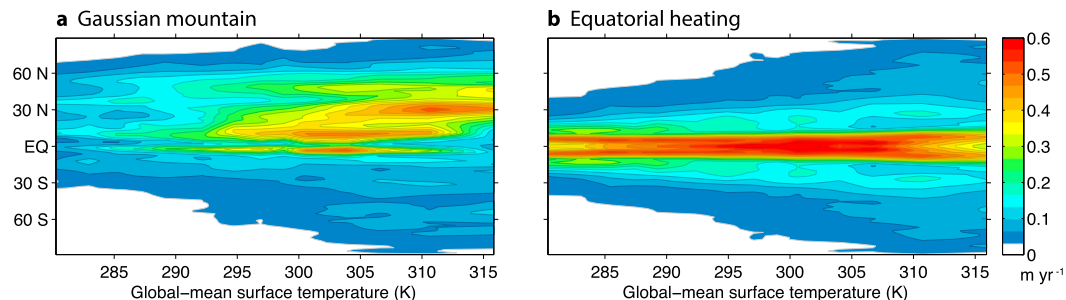


FIG. 5. Root zonal hydrological cycle variance, $\text{rms}(\overline{P^*} - \overline{E^*})$, vs latitude and global-mean surface temperature across the range of climates for (a) the Gaussian mountain experiment and (b) the equatorial heating experiment. Note that values have been symmetrized about the equator for the equatorial heating experiment.

idealized experiments. The zonally anomalous moisture budget can be written as

$$\bar{P}^* - \bar{E}^* = -\nabla \cdot \langle \bar{\mathbf{u}}\bar{q} \rangle^*, \quad (8)$$

where $\mathbf{u} = (u, v)$ is the horizontal wind, q is the specific humidity, ∇ is the nabla operator on a sphere, and $\langle \cdot \rangle$ is a mass-weighted vertical integral over atmospheric columns. While the native coordinates of the idealized GCM are sigma coordinates, we interpolate output to pressure coordinates to evaluate Eq. (8) and decompose fluxes into mean-flow and eddy components.³ This facilitates comparison with WS15, where the same analysis is performed with reanalysis data in pressure coordinates. We use 40 pressure levels, extending down to 1025 hPa, such that transient high pressure systems are also included in the analysis.

The total moisture flux convergence can be split into a component due to the time-mean flow (stationary eddies) and a component due to transient eddies. We define departures from the time mean as $(\cdot)' = (\cdot) - \overline{(\cdot)}$, such that

$$\bar{P}^* - \bar{E}^* = -\nabla \cdot \langle \bar{\mathbf{u}}\bar{q} + \overline{\mathbf{u}'q'} \rangle^*. \quad (9)$$

The stationary-eddy moisture flux convergence, $-\nabla \cdot \langle \bar{\mathbf{u}}\bar{q} \rangle^*$, can be further split into an advective and divergent component:

$$-\nabla \cdot \langle \bar{\mathbf{u}}\bar{q} \rangle^* = -\langle \bar{\mathbf{u}} \cdot \nabla \bar{q} + \bar{q} \nabla_\rho \cdot \bar{\mathbf{u}} \rangle^*. \quad (10)$$

Here ∇_ρ differs from ∇ in that it is weighted by an effective density, which vanishes on ‘‘underground’’ isobars. That is,

$$\nabla_\rho \cdot (\cdot) = \frac{1}{\bar{\rho}_\beta} \nabla \cdot (\bar{\rho}_\beta \cdot), \quad (11)$$

where

$$\bar{\rho}_\beta = \begin{cases} 1 & p < p_s \\ 0 & p > p_s \end{cases} \quad (12)$$

is the dimensionless density in pressure coordinates (cf. Boer 1982).

The transient-eddy term, $-\nabla \cdot \langle \overline{\mathbf{u}'q'} \rangle^*$, the full stationary-eddy term, $-\nabla \cdot \langle \bar{\mathbf{u}}\bar{q} \rangle^*$, the divergent stationary-eddy

term, $-\langle \bar{q} \nabla_\rho \cdot \bar{\mathbf{u}} \rangle^*$, and the advective stationary-eddy term, $-\langle \bar{\mathbf{u}} \cdot \nabla \bar{q} \rangle^*$, are shown in Fig. 6 for the reference climate of each experiment. As in the reanalysis (WS15), the divergent stationary-eddy term accounts for nearly all variance in $\bar{P}^* - \bar{E}^*$ between the equator and 30° or 40° latitude in both experiments. The reason this balance is possible despite large moisture tendencies associated with the transient-eddy and advective stationary-eddy terms is that the combined transient-eddy and advective term, $-\langle \bar{\mathbf{u}} \cdot \nabla \bar{q} + \nabla \cdot \overline{\mathbf{u}'q'} \rangle^*$, is small (Fig. 6). This is consistent with the mechanism discussed by WS15, where transient eddies relax moisture gradients set up by horizontal stationary-eddy moisture advection.

Also as in reanalysis, the divergent stationary-eddy term is almost entirely due to zonal anomalies in stationary-eddy mass convergence, $-\langle [\bar{q}] \nabla_\rho \cdot \bar{\mathbf{u}} \rangle^*$, rather than zonal anomalies in specific humidity, $-\langle \bar{q}^* \nabla_\rho \cdot \bar{\mathbf{u}} \rangle^*$, with the former accounting for more than 99% of the variance in the divergent stationary-eddy term. Figure 7 shows this and further approximations to the resulting dominant moisture balance. This dominant balance provides an excellent approximation for $\bar{P}^* - \bar{E}^*$ at latitudes up to 30° or 40° and continues to get the correct sign at higher latitudes.

The moisture budget decomposition shown here differs slightly from those of Newman et al. (2012) and WS15. Newman et al. (2012) puts the ∇_ρ in the advective term instead of the divergent term. WS15 does not use ∇_ρ in either term and instead defines an additional surface term that captures all effects of the spatiotemporal variability of surface pressure. These differences in formulation are only significant in regions where pressure levels intersect topographic slopes. The decomposition shown here has the advantage that $\nabla_\rho \cdot \bar{\mathbf{u}} = -(1/\bar{\rho}_\beta) \partial_p (\bar{\rho}_\beta \bar{\omega})$, by continuity. This leads to the property that an integral of the divergence up to level p_i gives the pressure velocity at p_i ,

$$\langle \nabla_\rho \cdot \bar{\mathbf{u}} \rangle_{p_i} = \frac{1}{g} \bar{\omega}|_{p_i}. \quad (13)$$

In contrast,

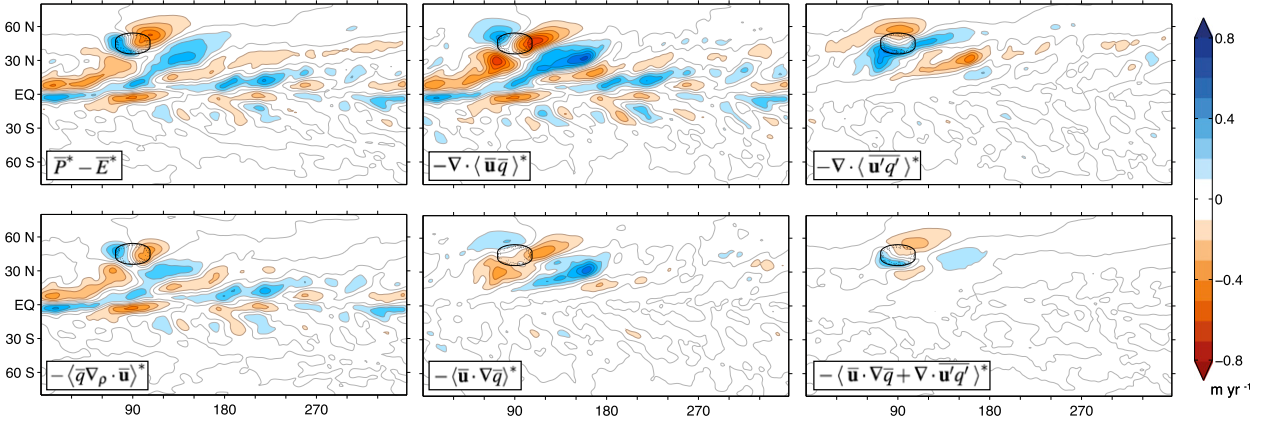
$$\langle \nabla \cdot \bar{\mathbf{u}} \rangle_{p_i} = \frac{1}{g} (\bar{\omega}|_{p_i} - \bar{\omega}_{\text{sfc}}), \quad (14)$$

where there is an additional term, $\bar{\omega}_{\text{sfc}} = \bar{\mathbf{u}}_{\text{sfc}} \cdot \nabla \bar{p}_s$, due to topographic slopes. The density-weighted divergence effectively combines the surface term and the stationary-eddy divergence term of WS15.

We can take advantage of the relationship between horizontal divergence and vertical velocity in Eq. (13) to derive a simple approximation for $\bar{P}^* - \bar{E}^*$ if we take $[\bar{q}]$

³ The mass-weighted vertical integral of each field is linearly interpolated from sigma to pressure coordinates at each time step such that the interpolation conserves mass. This is necessary in order to properly account for surface pressure fluctuations. Errors when interpolating after time averaging are of order 0.1–0.2 m yr^{-1} .

a Gaussian mountain



b Equatorial heating

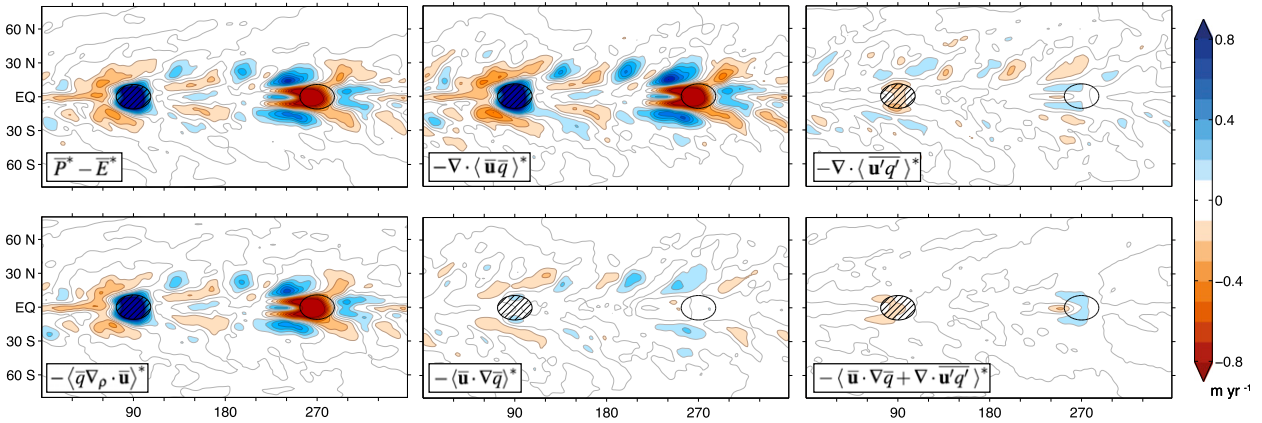


FIG. 6. Moisture budget terms in the reference climate ($\alpha = 1$) of (a) the Gaussian mountain experiment and (b) the equatorial heating experiment: zonally anomalous net precipitation ($\bar{P}^* - \bar{E}^*$), the total zonally anomalous moisture flux convergence by stationary eddies ($-\langle \nabla \cdot \bar{\mathbf{u}} \bar{q} \rangle^*$), the zonally anomalous moisture flux convergence by transient eddies ($-\langle \nabla \cdot \bar{\mathbf{u}}' q' \rangle^*$), the divergent component of the stationary-eddy moisture flux convergence ($-\langle \bar{q} \nabla_\rho \cdot \bar{\mathbf{u}} \rangle^*$), the advective component of the stationary-eddy moisture flux convergence ($-\langle \bar{\mathbf{u}} \cdot \nabla \bar{q} \rangle^*$), and the net zonally anomalous moisture tendency from transient-eddy moisture fluxes and stationary-eddy moisture advection ($-\langle \bar{\mathbf{u}} \cdot \nabla \bar{q} + \nabla \cdot \bar{\mathbf{u}}' q' \rangle^*$). (See Fig. 1 text for reference contour information.)

out of the vertical integral. This can be done with the integral mean value theorem, whereby

$$\langle [\bar{q}] \nabla_\rho \cdot \bar{\mathbf{u}} \rangle = [\bar{q}_{\text{sfc}}] \langle \nabla_\rho \cdot \bar{\mathbf{u}} \rangle_{p_i} \quad (15)$$

for some level p_i in the vertical domain. We calculate the pressure p_i for which Eq. (15) holds exactly at every grid point in each simulation. The global-mean p_i in the reference climate is 860 hPa (orographic forcing) and 840 hPa (equatorial heating). We then approximate this relation by using one value, $p_i = 850$ hPa, globally in both experiments. The best-fit value of p_i is shown versus latitude for all simulations in Fig. 8. The best-fit value of p_i in the subtropics and midlatitudes is seen to decrease as the climate warms and the depth of the troposphere and the water vapor-scale height increase.

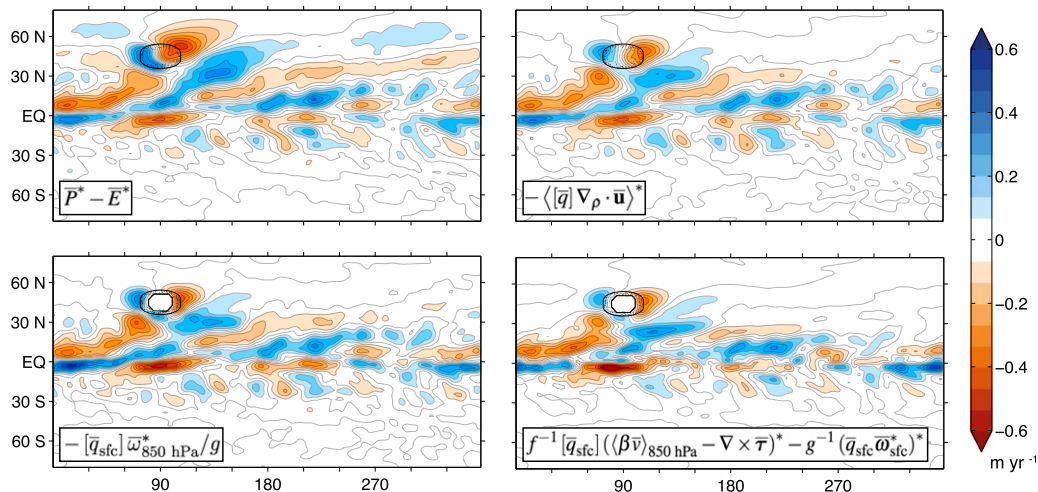
Equations (13) and (15) imply that zonal variation in $\bar{P} - \bar{E}$ is primarily determined by a product of the

zonal-mean surface specific humidity and the zonally anomalous vertical motion at 850 hPa:

$$\bar{P}^* - \bar{E}^* \approx -\frac{1}{g} [\bar{q}_{\text{sfc}}] \bar{\omega}_{850 \text{ hPa}}^* \quad (16)$$

This is shown for the reference simulations in Fig. 7. The approximation captures all features of $\bar{P}^* - \bar{E}^*$ in the tropics and subtropics, up to 30° latitude. It starts to break down at higher latitudes, but still generally captures the sign of $\bar{P}^* - \bar{E}^*$. This approximation should not be taken too literally directly over the mountain, where the local \bar{q}_{sfc} is drastically different from the zonal mean. It is undefined for a small region around the peak of the mountain where the surface extends above 850 hPa. This approximation is identical to that used in WS15 with reanalysis data, despite slight differences in the moisture budget decomposition.

a Gaussian mountain



b Equatorial heating

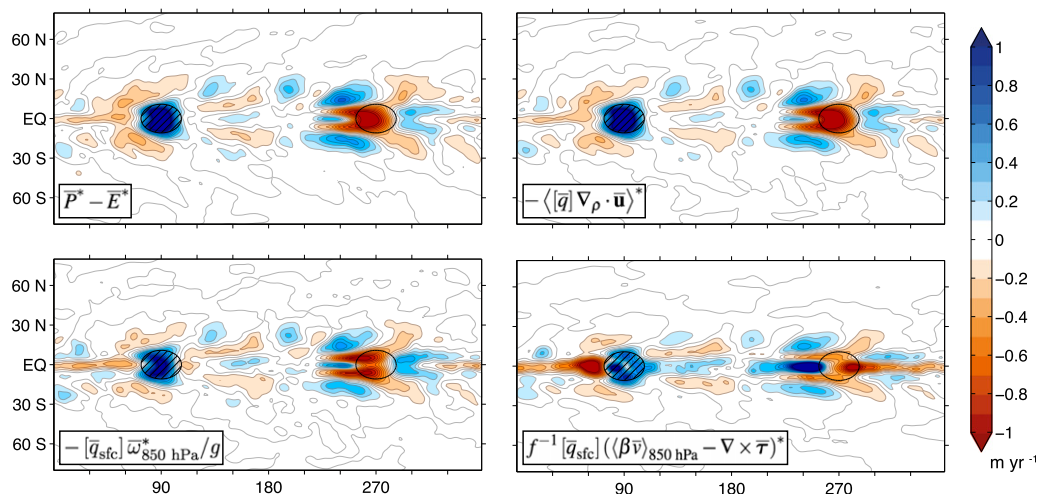


FIG. 7. Moisture budget terms in the reference climate ($\alpha = 1$) of (a) the Gaussian mountain experiment and (b) the equatorial heating experiment: $\bar{P}^* - \bar{E}^*$ and approximations to $-\langle [\bar{q}] \nabla \rho \cdot \bar{\mathbf{u}} \rangle^*$, the dominant term determining $\bar{P}^* - \bar{E}^*$. (See Fig. 1 text for reference contour information.)

b. Vorticity constraints on vertical motion

Stationary Rossby wave theory (e.g., Hoskins and Karoly 1981) usually solves for the Rossby wave response to zonally asymmetric topography or heating in terms of a horizontal streamfunction. To understand how this horizontal flow is related to the stationary-eddy vertical motion that determines $\bar{P}^* - \bar{E}^*$, it is useful to analyze the zonally anomalous vorticity equation. We focus on the zonally anomalous vorticity budget below 850 hPa, which can be written as

$$\langle f \nabla \cdot \bar{\mathbf{u}} + \beta \bar{v} + \bar{N} \rangle_{850 \text{ hPa}}^* = \nabla \times \bar{\boldsymbol{\tau}}^*, \quad (17)$$

where f is the Coriolis frequency, $\beta = df/dy$, $\boldsymbol{\tau}$ is the turbulent surface stress, and

$$N = \mathbf{v} \cdot \nabla \zeta + \zeta \nabla \cdot \mathbf{u} + (\nabla_x \cdot \boldsymbol{\omega}) \partial_p v - (\nabla_y \cdot \boldsymbol{\omega}) \partial_p u \quad (18)$$

is the sum of all nonlinear (relative vorticity) terms. This uses the fact that 850 hPa is above the Ekman layer throughout the range of climates.

The terms of the vorticity equation in Eq. (17), weighted by $[\bar{q}_{\text{sfc}}]/f$, are shown in Fig. 9, such that the plotted fields are in units of meters per year. In this way, each term is a contribution to $\bar{P}^* - \bar{E}^*$, as, for example,

$$-\langle [\bar{q}] \nabla \cdot \bar{\mathbf{u}} \rangle^* \approx -\frac{[\bar{q}_{\text{sfc}}]}{f} \langle f \nabla \cdot \bar{\mathbf{u}} \rangle_{850 \text{ hPa}}^*. \quad (19)$$

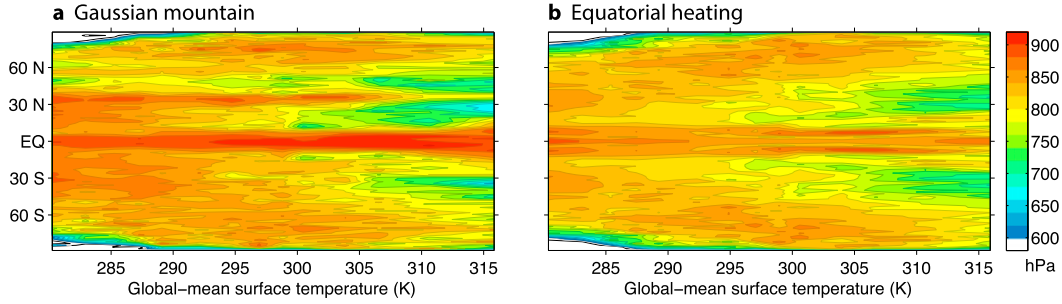


FIG. 8. Zonal-mean best-fit p_i from Eq. (15) for (a) the Gaussian mountain experiment and (b) the equatorial heating experiment. Note that values have been symmetrized about the equator for the equatorial heating experiment.

Note that this differs from $-\langle[\bar{q}]\nabla_p \cdot \bar{\mathbf{u}}\rangle^*$ by an additional term

$$\begin{aligned} (\bar{P}^* - \bar{E}^*)_{\text{orographic}} &\equiv -\langle\bar{q}\nabla_p \cdot \bar{\mathbf{u}}\rangle^* + \langle\bar{q}\nabla \cdot \bar{\mathbf{u}}\rangle^* \\ &\approx -\langle[\bar{q}]\nabla_p \cdot \bar{\mathbf{u}}\rangle^* + \langle[\bar{q}]\nabla \cdot \bar{\mathbf{u}}\rangle^*, \end{aligned} \quad (20)$$

arising from the difference in density weighting between the moisture and vorticity budgets. This term is equivalent to the surface term defined in WS15. It means that, in addition to the stationary-eddy vertical velocities based on the vorticity budget, there is a vertical velocity $\bar{\omega}_{\text{sfc}}^* = (\bar{\mathbf{u}}_{\text{sfc}} \cdot \nabla \bar{p}_s)^*$, which contributes to $\bar{P}^* - \bar{E}^*$ as surface moisture fluxes converge onto sloped surfaces⁴:

$$(\bar{P}^* - \bar{E}^*)_{\text{orographic}} \approx -\frac{1}{g}(\bar{q}_{\text{sfc}} \bar{\omega}_{\text{sfc}}^*)^*. \quad (21)$$

This term is shown in Fig. 10 for the Gaussian mountain experiment.

The dominant vorticity balance determining vertical motion at 850 hPa in both experiments is through the linear (planetary vorticity) terms and surface drag, a combination of Sverdrup balance and Ekman pumping:

$$-\langle f \nabla \cdot \bar{\mathbf{u}} \rangle_{850 \text{ hPa}}^* \approx \langle \beta \bar{v} \rangle_{850 \text{ hPa}}^* - \nabla \times \bar{\boldsymbol{\tau}}^*. \quad (22)$$

The nonlinear terms do not play a large role in the orographic forcing experiments. The nonlinear terms are more important in the tropical heating experiments where they redistribute vorticity along the equator. This agrees well with the analysis of reanalysis data in WS15, where the nonlinear vorticity terms are seen to be

mainly important for redistributing vorticity within the tropical Pacific.

The linear vorticity balance can be used to develop an approximation for $\bar{P}^* - \bar{E}^*$ that emphasizes the role of the horizontal flow in stationary eddies:

$$\bar{P}^* - \bar{E}^* = \frac{[\bar{q}_{\text{sfc}}]}{f} (\langle \beta \bar{v} \rangle_{850 \text{ hPa}} - \nabla \times \bar{\boldsymbol{\tau}})^* - \frac{1}{g} (\bar{q}_{\text{sfc}} \bar{\omega}_{\text{sfc}}^*)^*, \quad (23)$$

which is shown for the reference simulations in Fig. 7. This approximation results in the interpretation that regions of low-level poleward or cyclonic flow are wetter than the zonal mean, while regions of low-level equatorward or anticyclonic flow are drier than the zonal mean. The individual components of this approximation, shown in Fig. 9, can be thought of separately as the contributions of meridional motion and surface drag to $\bar{P}^* - \bar{E}^*$. The orographic $\bar{\omega}_{\text{sfc}}$ term (Fig. 10) is only important over large gradients of surface pressure, as exist immediately over topography.

The approximations for $\bar{P}^* - \bar{E}^*$ developed here [Eqs. (16) and (23), Fig. 7] can be used to understand the response of $\bar{P}^* - \bar{E}^*$ to climate change in these experiments.

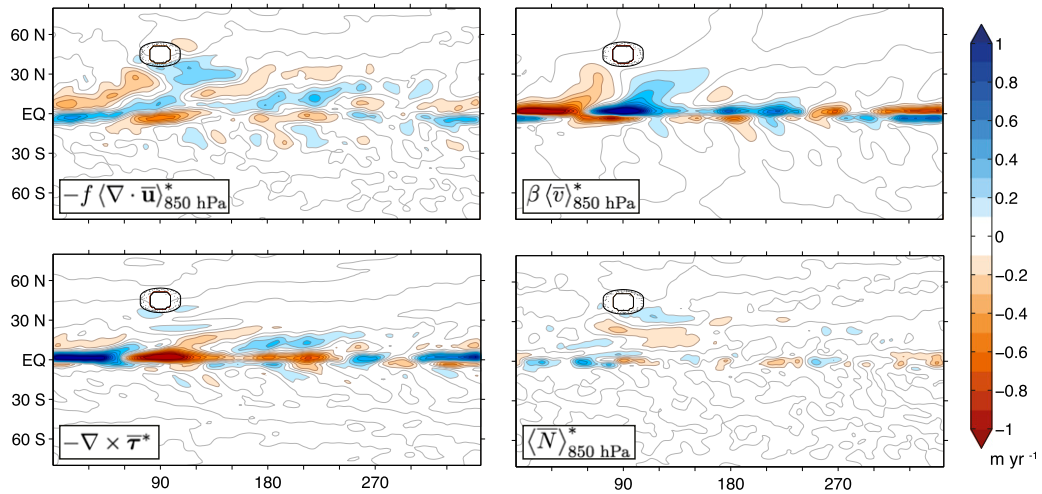
5. Mechanisms of zonally anomalous hydrological cycle change

a. Thermodynamic and dynamic changes

The arguments of section 2 have already suggested that changes in circulation are important for changes in $\bar{P}^* - \bar{E}^*$. This conclusion is further strengthened by looking at the change in the stationary-eddy vertical velocity and its effect on $\bar{P}^* - \bar{E}^*$ according to the approximation in Eq. (16). The change in this approximation explains most of the change in $\bar{P}^* - \bar{E}^*$ (cf. Fig. 11 and Fig. 3). The $\bar{P}^* - \bar{E}^*$ change approximation

⁴ While it is a good approximation to use $[\bar{q}]$ in Eq. (20), $[\bar{q}_{\text{sfc}}]$ should not be used in Eq. (21), because \bar{q}_{sfc} has large spatial gradients over topography due to spatial variation of surface pressure.

a Gaussian mountain



b Equatorial heating

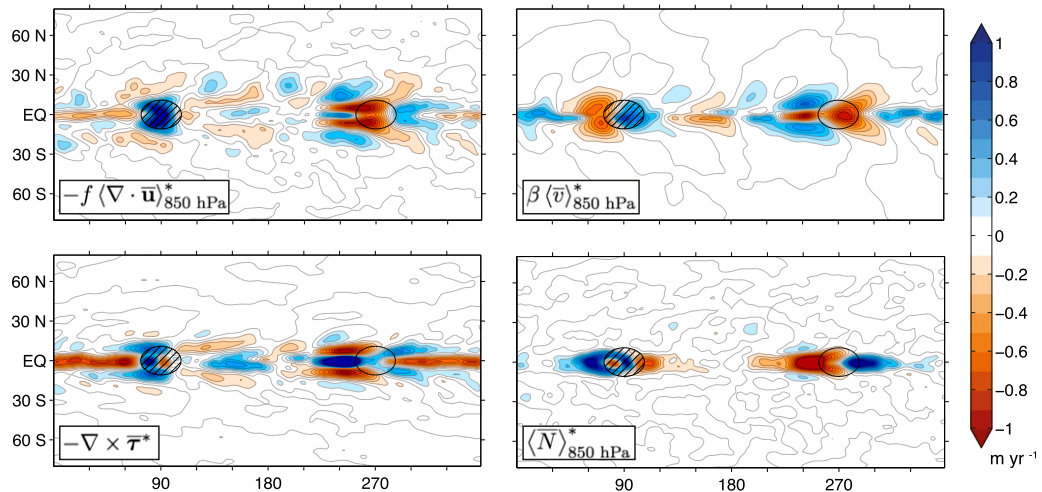


FIG. 9. Moisture-weighted lower-tropospheric vorticity budget terms in the reference climate ($\alpha = 1$) of (a) the Gaussian mountain experiment and (b) the equatorial heating experiment. All terms are multiplied by $[\bar{q}_{\text{sfc}}]/f$ such that they show a contribution to $\bar{P}^* - \bar{E}^*$. Note that $(\bar{N})^*$ is computed as a residual of the other terms. (See Fig. 1 text for reference contour information.)

can be split into thermodynamic and dynamic components as

$$\begin{aligned} \delta(\bar{P}^* - \bar{E}^*) \approx & -g^{-1}[\bar{q}_{\text{sfc}}]_0 \delta\bar{\omega}_{850\text{hPa}}^* \quad (\text{dynamic}) \\ & -g^{-1}\delta[\bar{q}_{\text{sfc}}](\bar{\omega}_{850\text{hPa}}^*)_0 \quad (\text{thermodynamic}) \\ & -g^{-1}\delta[\bar{q}_{\text{sfc}}]\delta\bar{\omega}_{850\text{hPa}}^* \quad (\text{product}), \end{aligned} \quad (24)$$

which are shown in Fig. 11. In most regions, the dynamic change leads to a larger change in $\bar{P}^* - \bar{E}^*$ than the thermodynamic change. This is surprising since the dynamic change is not directly related to the increase in atmospheric moisture content, which is large due to the C–C relation ($\sim 35\%$ in the tropics for the increase in

global-mean surface temperature of 5.7 K shown in Fig. 11). Not only is the thermodynamic change smaller, but it is mostly out of phase with the full change. The product of changes in moisture and vertical motion ($-\delta[\bar{q}_{\text{sfc}}]\delta\bar{\omega}_{850\text{hPa}}^*$) looks like the dynamic change, but is approximately 3 times smaller, accounting for the interactions of the $\sim 35\%$ change in specific humidity with the modified stationary-eddy circulations. In this way, changes in $\bar{P}^* - \bar{E}^*$ in these idealized experiments are primarily determined by changes in $\bar{\omega}_{850\text{hPa}}^*$.

In comparing with $\bar{P}^* - \bar{E}^*$ changes in the full climate system, the idealizations of this setup should be kept in mind. In particular, these idealized GCM simulations have no land–sea thermal contrast or seasonal cycle.

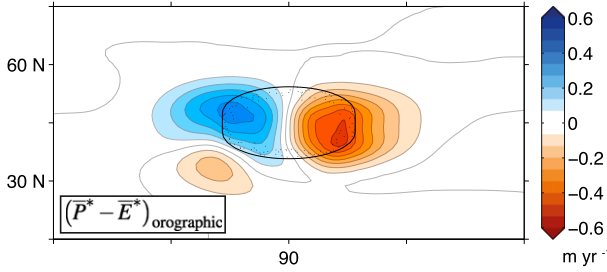


FIG. 10. Orographic contribution to $\overline{P^*} - \overline{E^*}$ in the Gaussian mountain experiment, calculated here from $-\langle[\overline{q}]\nabla_p \cdot \overline{\mathbf{u}}\rangle^* + \langle[\overline{q}]\nabla \cdot \overline{\mathbf{u}}\rangle^*$. This term is already accounted for in the moisture budget approximation in Eq. (16), but must be added to an approximation based on the vorticity budget in Eq. (23).

WS15 have examined the robustness of the vertical motion approximation [Eq. (16)] over the seasonal cycle in ERA-Interim reanalysis of the last 35 years. While the divergent vertical motion term is still the dominant contribution to $\overline{P^*} - \overline{E^*}$, stationary-eddy moisture advection and transient-eddy moisture fluxes become more important seasonally, especially over regions of ocean heat uptake/release in the high latitudes and over North America. Southern North America is moistened by transient eddies (relative to the zonal mean) in December–February (DJF), and the west coast is kept dry by stationary-eddy moisture advection in June–August (JJA). Seager et al. (2014b) examines these North American moisture balances for climate change in CMIP5 models, finding that the winter $\overline{P} - \overline{E}$ changes are a superposition of transient-eddy changes, divergent circulation changes, and dynamic and thermodynamic advection changes and that the summer $\overline{P} - \overline{E}$ changes on the west coast are small due to a cancellation of thermodynamic and dynamic changes in stationary-eddy moisture advection. However, an analogous analysis of $\overline{P} - \overline{E}$ in the Mediterranean region shows the importance of the divergent circulation changes (Seager et al. 2014a), as in our idealized GCM analysis. In general, the value of the vertical motion approximation for assessing $\overline{P^*} - \overline{E^*}$ changes is greatest in the tropics and subtropics away from topography.

b. Changes in zonal variance of net precipitation

With an understanding of the importance of $\overline{\omega}_{850\text{hPa}}^*$ for changes in $\overline{P^*} - \overline{E^*}$, we return to the question of the dynamics controlling changes in amplitude of zonal hydrological cycle variations, $\text{rms}(\overline{P^*} - \overline{E^*})$ (Figs. 4 and 5). To study $\text{rms}(\overline{P^*} - \overline{E^*})$ over the full range of climates, we average it over several latitude bands (Figs. 12). The change in $\text{rms}(\overline{P^*} - \overline{E^*})$ in each latitude band can be compared to the change in surface specific humidity (Fig. 12, blue lines), which approximately follows the C–C relation.

The $\text{rms}(\overline{P^*} - \overline{E^*})$ equatorward of the topographic forcing, between 10° and 30°N (Fig. 12b), exceeds the C–C surface specific humidity line in climates warmer than the reference simulation (289-K global-mean surface temperature), then returns to the C–C line before decreasing in climates warmer than 304-K global-mean surface temperature. The climate becomes more zonal for these very warm climates, leading to the opposite response of $\text{rms}(\overline{P^*} - \overline{E^*})$ from what would be expected under *wet gets wetter, dry gets drier*. The change is similar for $\text{rms}(\overline{P^*} - \overline{E^*})$ in the deep tropics of this experiment ($2^\circ < |\phi| < 10^\circ$): it stays close to the C–C line before decreasing rapidly in very warm climates (Fig. 12c). The $\text{rms}(\overline{P^*} - \overline{E^*})$ in the Southern Hemisphere subtropics (30°–10°S, Fig. 12d), resulting from tunneling of Rossby waves across the equator, and in the midlatitudes in the vicinity of topography (30°–60°N, Fig. 12a), are limited by dynamic stationary-wave changes and do not increase as rapidly as predicted from C–C.

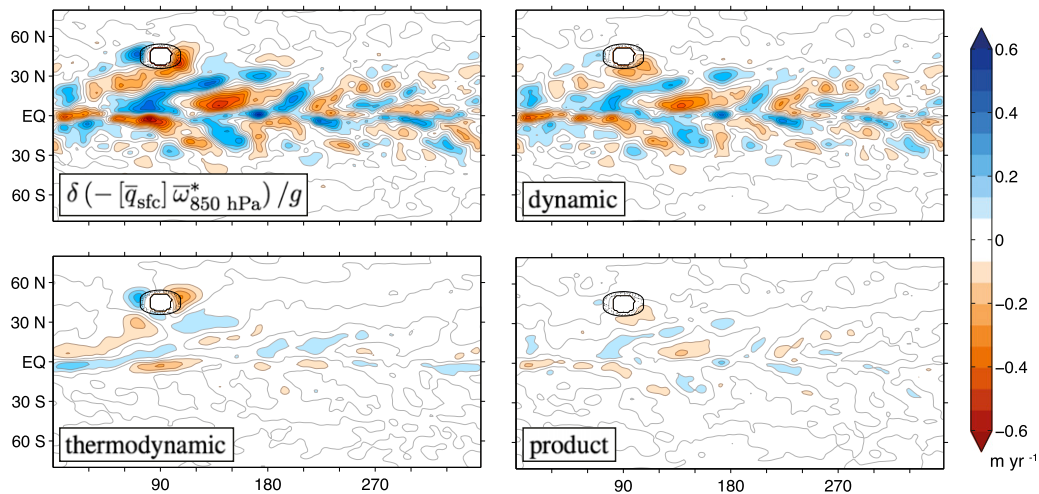
The $\text{rms}(\overline{P^*} - \overline{E^*})$ in the deep tropics of the equatorial heating experiment increases much more slowly than expected from C–C (Fig. 12e). This results from a slowdown of the Walker circulation, which helps to satisfy global energetic constraints on the total upward mass transport of the atmosphere (Betts 1998; Held and Soden 2006; Vecchi and Soden 2007; Schneider et al. 2010). This slowdown of the Walker circulation is reflected in the $\text{rms}(\overline{P^*} - \overline{E^*})$ up to at least 30° latitude (Fig. 12f). In the extratropics (30°–60°, Fig. 12g), $\text{rms}(\overline{P^*} - \overline{E^*})$ increases somewhat more slowly than surface specific humidity, as seen in Fig. 4, and stops increasing beyond about 300-K global-mean surface temperature. The dynamic limitation in the midlatitudes of this experiment could result from an influence of the Walker circulation on stationary eddies in midlatitudes, or a local influence of the increased static stability.

Changes in $\text{rms}(\overline{P^*} - \overline{E^*})$ are well described by changes in rms of the $\overline{P^*} - \overline{E^*}$ approximation [Eq. (16)]:

$$\text{rms}(\overline{P^*} - \overline{E^*}) \approx \frac{1}{g} [\overline{q}_{\text{sfc}}] \text{rms}(\overline{\omega}_{p_i}^*). \quad (25)$$

This scaling is shown as dashed black lines in Fig. 12. We choose p_i separately for each latitude band to minimize the difference between $g^{-1}[\overline{q}_{\text{sfc}}] \text{rms}(\overline{\omega}_{p_i}^*)$ and $\text{rms}([\overline{q}]\nabla \cdot \overline{\mathbf{u}}^*)$, roughly following the zonal-mean p_i shown in Fig. 8. The scaling is only marginally more successful when using a p_i that varies with climate, so we keep p_i fixed for simplicity. The main influence of changes in p_i is on the subtropics of the orographic forcing experiment, where almost all differences between the $\overline{P^*} - \overline{E^*}$ variance and the approximation based on the $\overline{\omega}_{p_i}^*$ variance are due to the assumption of

a Gaussian mountain



b Equatorial heating

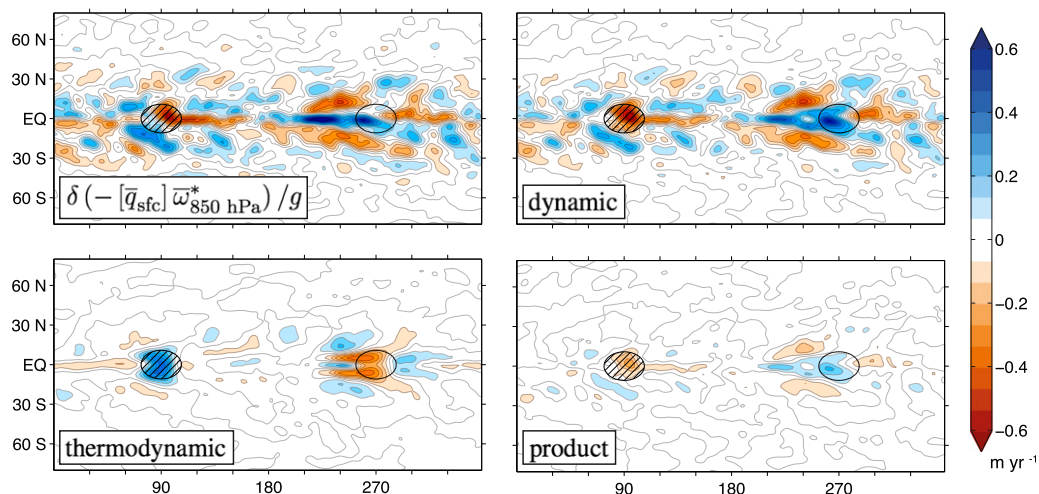


FIG. 11. Change in the scaling for $\bar{P}^* - \bar{E}^*$, $\delta(-[\bar{q}_{\text{sfc}}]\bar{\omega}_{850}^*)/g$, from the reference climate ($\alpha = 1$) to the climate with 1.4 times the optical depth ($\alpha = 1.4$). (a) Gaussian mountain experiment. (b) Equatorial heating experiment. The changes are split into a thermodynamic component, based on changes in $[\bar{q}_{\text{sfc}}]$, a dynamic component, based on changes in $\bar{\omega}_{850}^*$, and a product of these changes. (See Fig. 1 text for reference contour information.)

fixed p_i , because p_i , the representative height for condensation in vertical motion, moves upward with warming.

Because the zonal-mean surface specific humidity is not a representative value of specific humidity directly over topography (the height of topography is comparable to the water vapor–scale height), this scaling is modified over topography to use the full surface specific humidity:

$$\text{rms}(\bar{P}^* - \bar{E}^*) \approx \frac{1}{g} \text{rms}(\bar{q}_{\text{sfc}} \bar{\omega}_{p_i}^*), \quad (26)$$

which is shown as a dashed black line in Fig. 12a. This modification makes a noticeable difference here, but could

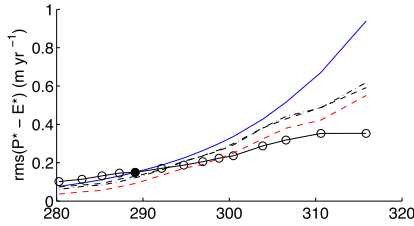
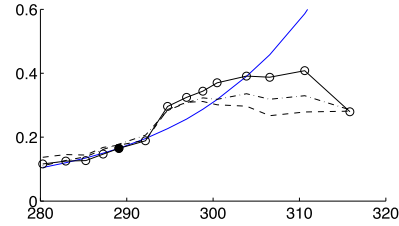
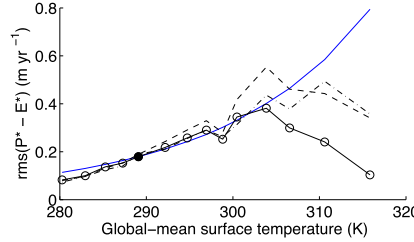
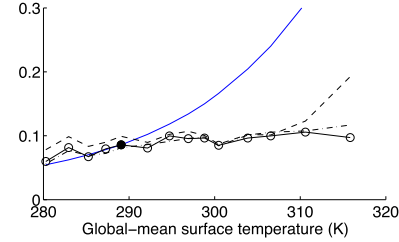
probably be avoided for topography that does not extend above 850 hPa or have such a large zonal scale. The difference between $\text{rms}(\bar{q}_{\text{sfc}} \bar{\omega}_{p_i}^*)$ and $\text{rms}(\bar{P}^* - \bar{E}^*)$ in mid-latitudes shows that transient eddies increase $\bar{P}^* - \bar{E}^*$ variance in cold climates (i.e., through creation of a storm track) and decrease variance in warm climates (through downgradient moisture fluxes).

A scaling for $\text{rms}(\bar{P}^* - \bar{E}^*)$ based on the linear vorticity balance in Eq. (23),

$$\text{rms}(\bar{P}^* - \bar{E}^*) \sim \frac{[\bar{q}_{\text{sfc}}]}{f} \text{rms}((\beta \bar{v})_{p_i}^* + \nabla \times \bar{\tau}^*), \quad (27)$$

is shown as dash-dotted lines in Fig. 12. Again, we must modify the scaling in the vicinity of large topography:

Gaussian mountain

a 30°N - 60°N, $p_i = 750$ hPab 10°N - 30°N, $p_i = 800$ hPac 2° - 10°, $p_i = 900$ hPad 30°S - 10°S, $p_i = 800$ hPa

— $[\bar{q}_{\text{sfc}}]$
 ○ $\text{rms}(\bar{P}^* - \bar{E}^*)$
 - - - $g^{-1} [\bar{q}_{\text{sfc}}] \text{rms}(\bar{\omega}_{p_i}^*)$
 - · - · $g^{-1} [\bar{q}_{\text{sfc}}] \text{rms}(\bar{\omega}_{\text{vort}}^*)$
 - - - $g^{-1} \text{rms}(\bar{q}_{\text{sfc}} \bar{\omega}_{\text{sfc}}^*)$

Equatorial heating

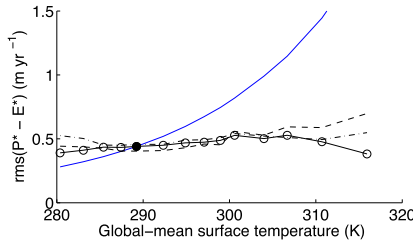
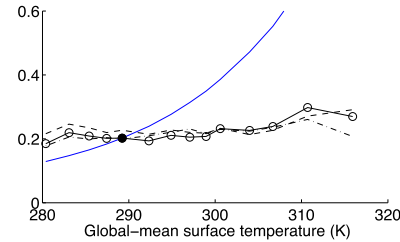
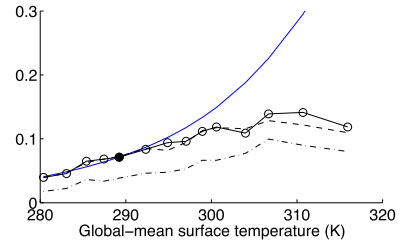
e 2° - 10°, $p_i = 850$ hPaf 10° - 30°, $p_i = 800$ hPag 30° - 60°, $p_i = 750$ hPa

FIG. 12. Root zonal hydrological cycle variance, $\text{rms}(\bar{P}^* - \bar{E}^*)$, within a latitude band (solid line with circles) and scalings for it based on the flow divergence below p_i (dashed line), based on the linear vorticity balance, $\bar{\omega}_{\text{vort}}^* = \langle \beta \bar{v} \rangle_{p_i}^* - \nabla \times \bar{\tau}^* - f \bar{\omega}_{\text{sfc}}^*$ (dash-dotted line), and based on $\bar{\omega}_{\text{sfc}}^*$ over topography (red dashed line). The approximately exponential change in $\text{rms}(\bar{P}^* - \bar{E}^*)$ expected from a purely thermodynamic change of surface specific humidity is shown as a blue line. Averages over (a) 30°–60°N, (b) 10°–30°N, (c) $\pm 2^\circ$ –10°, and (d) 30°–10°S in the Gaussian mountain experiment and (e) $\pm 2^\circ$ –10°, (f) $\pm 10^\circ$ –30°, and (g) $\pm 30^\circ$ –60° in the equatorial heating experiment. The pressure p_i (shown above each subpanel) is chosen for each latitude band separately as described in the text.

$$\text{rms}(\bar{P}^* - \bar{E}^*) \sim \frac{1}{f} \text{rms} \left[\bar{q}_{\text{sfc}} \left(\langle \beta \bar{v} \rangle_{p_i}^* + \nabla \times \bar{\tau}^* - \frac{f}{g} \bar{\omega}_{\text{sfc}}^* \right) \right]. \quad (28)$$

This scaling is also successful at all latitudes, especially in the subtropics, where nonlinear vorticity tendencies are small.⁵ It is surprising that these scalings are successful for the midlatitudes of the orographic forcing experiment, where transient-eddy moisture tendencies are most significant. This success comes from the orographic vertical velocity term [$\text{rms}(\bar{q}_{\text{sfc}} \bar{\omega}_{\text{sfc}}^*)$, red

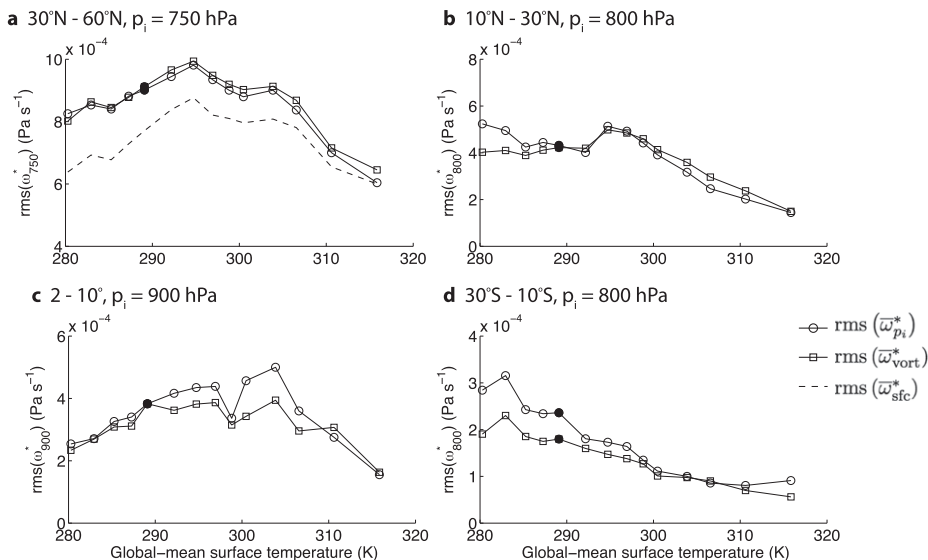
line in Fig. 12a], which explains a large portion of the variance.

The dynamic components of the precipitation variance scalings in Eqs. (25), (26) and (27), (28) are shown in Fig. 13. In the orographic forcing experiment, stationary-eddy vertical motion changes nonmonotonically, with a slight increase in variance with warming through the colder climates and a strong decrease in variance in the warmest climates (Figs. 13a–c), especially in midlatitudes. This reflects the $\bar{\omega}_{\text{sfc}}^*$ variance (dashed line, Fig. 13a), which is responsible for forcing the topographic stationary wave through adiabatic heating and cooling on the topographic slope. The vertical-motion variance in the Southern Hemisphere subtropics (Fig. 13d) behaves differently, decreasing with warming throughout the range of climates.

The stationary-eddy vertical-motion changes in the equatorial heating experiment show the weakening of

⁵The nearest grid point to the equator in each hemisphere is excluded from this analysis because it causes problems with the vorticity-budget scaling due to strong nonlinear vorticity tendencies (cf. Fig. 9).

Gaussian mountain



Equatorial heating

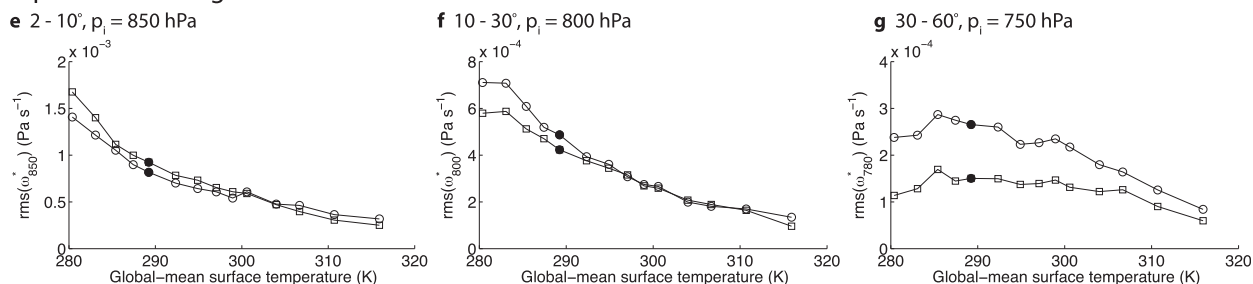


FIG. 13. Contribution to the scalings of Fig. 12 from $\text{rms}(\overline{\omega_{p_i}^*})$ (circles) and the estimate of $\text{rms}(\overline{\omega_{p_i}^*})$ based on $\overline{\omega_{vort}^*} = (\beta \overline{v})_{p_i}^* - \nabla \times \overline{\tau}^* - f \overline{\omega_{sfc}^*}$ (squares) are shown for (a) 30°–60°N, (b) 10°–30°N, (c) $\pm 2^\circ$ –10°, and (d) 30°–10°S in the Gaussian mountain experiment and (e) $\pm 2^\circ$ –10°, (f) $\pm 10^\circ$ –30°, and (g) $\pm 30^\circ$ –60° in the equatorial heating experiment. Also shown in (a) is $\text{rms}(\overline{\omega_{sfc}^*})$ (dashed line), which determines much of the lower-tropospheric vertical velocity variance over topography. The pressure p_i is the same as in the corresponding experiment and latitude band in Fig. 12.

the Walker circulation and other tropical overturning circulations (Figs. 13e,f), which has been pointed out as a robust response to global warming (Held and Soden 2006; Vecchi et al. 2006; Vecchi and Soden 2007). Vertical motion variance also decreases in midlatitudes of the equatorial heating experiment (Fig. 13g) due to a combination of tropical Rossby wave source changes and changes in midlatitude isentropic slopes.

The key unanswered questions in understanding how the zonally anomalous hydrological cycle responds to global warming lie in understanding the stationary-eddy vertical-motion response. The response can mostly be understood from the perspective of a combined Sverdrup and Ekman balance [Eq. (28); squared lines in Fig. 13], relating the vertical motion to the lower-tropospheric meridional motion, surface wind stress curl, and surface vertical velocity. The question of how $\text{rms}(\overline{\omega_{p_i}^*})$ responds to climate change is thus also a

question of how the lower-level horizontal flow in stationary eddies responds to climate change. We discuss some of the dynamical questions raised by these experiments in the next section.

6. Discussion

The moisture budget decomposition of section 4 allows the change in $\overline{P}^* - \overline{E}^*$ in these two idealized model experiments to be understood in terms of simple thermodynamic changes and changes in lower-tropospheric stationary-eddy vertical motion. It is thus important to understand why lower-tropospheric stationary-eddy vertical motion changes as it does with climate change. The lower-level vorticity balance implies that most of these vertical motion changes are associated with changes in lower-tropospheric stationary-eddy horizontal motion. We thus discuss changes in the

lower-tropospheric manifestation of stationary eddies in these experiments.

While several studies have analyzed the stationary-eddy response to climate change using realistic forcing (Stephenson and Held 1993; Brandefelt and Körnich 2008; Simpson et al. 2014, 2016), the advantage of the idealized GCM experiments presented here is that we can separately analyze the Rossby wave response associated with topographic forcing and equatorial heating. We have already seen how these two types of forcing give different circulation responses to climate change in Fig. 13. We would like to understand which changes in the idealized climate with orographic forcing lead to an increase and then decrease of $\text{rms}(\overline{\omega}_{p_i}^*)$ with warming and which changes in the idealized climate with a Walker circulation lead to a decreasing $\text{rms}(\overline{\omega}_{p_i}^*)$ throughout the range of climates. We will restrict ourselves to a qualitative discussion here. A detailed quantitative analysis can be found in Wills (2016) and the associated forthcoming work.

a. Orographic forcing

A linear quasigeostrophic analysis of the response of stationary waves to topographic forcing identifies the low-level zonal wind as a key factor controlling the magnitude of response (Hoskins and Karoly 1981; Held and Ting 1990). The interaction of surface winds with a mountain of height h creates a vertical velocity $w_{\text{sfc}} = \mathbf{u}_{\text{sfc}} \cdot \nabla h$. The generation of the orographic vertical velocity w_{sfc} is dominated by the zonal-mean zonal wind component, $[\overline{u}_{\text{sfc}}] \partial_x h$, which responds nonmonotonically to climate change in these experiments, mirroring nonmonotonic changes in transient-eddy momentum-flux convergence (Levine and Schneider 2011). The adiabatic heating/cooling induced by this vertical velocity is primarily balanced by meridional advection, inducing a stationary-eddy wind $\overline{\mathbf{v}}^*$. The amplitude response of the resulting stationary wave to warming will thus depend on w_{sfc} , the thermodynamic structure of the atmosphere (i.e., meridional temperature gradients and static stability), and diabatic tendencies such as latent heating.

b. Walker circulation

The slowdown of the tropical overturning circulations, such as Walker circulations, with global warming is robust across many types of models and observations (Held and Soden 2006; Vecchi et al. 2006; Vecchi and Soden 2007; Merlis and Schneider 2011). Global energetic constraints on evaporation/precipitation lead to a reduction of the strength of overturning circulations globally in response to increases in the surface specific humidity or its lapse rate (Betts 1998; Held and Soden 2006; Vecchi and Soden 2007; Schneider et al. 2010).

Zonally anomalous circulations in the tropics make up 40% of the total overturning of the atmosphere in the equatorial heating experiments (calculated from the upward portion of $\overline{\omega}_{500}$), so the naive assumption would be that they account for 40% of the decrease in overturning resulting from energetic limitations. As pointed out by Held and Soden (2006) and Vecchi and Soden (2007), it is not unreasonable to think that even more of the decrease in overturning will be concentrated in the zonally anomalous circulations, since zonal-mean circulations (e.g., the Hadley cell) have to obey angular momentum constraints as well as energetic constraints. But the global energetic constraints do not provide a quantitative theory for the strength of zonal overturning circulations in particular. Local constraints can be obtained from the moisture budget, based on small changes in moisture-flux convergence (Merlis and Schneider 2011), or from the MSE equation, based on increasing gross moist stability with warming and the corresponding increased energetic requirements of deep convection (Chou and Neelin 2004).

c. Midlatitude isentropic slopes

An additional balance relating vertical and meridional motion in the extratropics exists through the thermodynamic equation, where meridional advection balances vertical advection of potential temperature in the absence of significant diabatic effects. In this way, stationary-eddy vertical velocities are related to stationary-eddy meridional velocities and the slope of isentropes. The reduction of isentropic slopes with warming provides another means for decreasing stationary-eddy vertical velocities, even without changes in the horizontal circulation. This mechanism contributes to the decrease of $\text{rms}(\overline{\omega}_{p_i}^*)$ in the Southern Hemisphere subtropics of the Gaussian mountain experiment (Fig. 13d) and in the midlatitudes of the equatorial heating experiment (Fig. 13g).

d. Upper-level wind

Because of the large range of climates simulated in these experiments, there are large changes in the upper-level winds. Rossby wave theory tells us that this could lead to changes in the wavenumber of Rossby waves that are stationary (Hoskins and Karoly 1981; Held 1983). However, due to the large zonal scale of the topographic and ocean heat-flux forcing used here, the dominant wavenumbers forced ($k = 1-4$) are stationary throughout the range of climates. The upper-level wind changes exert an influence on the spatial distribution of stationary-eddy circulations, but the amplitude is found to be controlled primarily by dynamics of the forcing regions, discussed above.

7. Conclusions

Based on moist idealized GCM simulations with zonally varying boundary conditions, we can draw several conclusions about how stationary eddies and zonal variations in the hydrological cycle respond to climate change:

- 1) Changes in $\bar{P}^* - \bar{E}^*$ are primarily determined by changes in lower-tropospheric stationary-eddy vertical motion.
- 2) Changes in stationary-eddy circulations are large such that *wet gets wetter, dry gets drier* ideas do not apply locally.
- 3) The zonal-mean spatial variance of $\bar{P}^* - \bar{E}^*$ increases with climate change at a rate near that determined by the Clausius–Clapeyron equation for climates with near-modern surface temperatures when stationary eddies are forced by midlatitude topography.
- 4) Topographic forcing has a reduced influence on zonal variations of the hydrological cycle for temperatures greater than 305 K in these simulations.
- 5) The zonal-mean spatial variance of $\bar{P}^* - \bar{E}^*$ hardly changes with climate change when stationary eddies are forced by equatorial heating, implying a strong weakening of the Walker circulation and other divergent stationary-eddy circulations with warming.

The zonal-mean spatial variance of $\bar{P}^* - \bar{E}^*$ in the real world will be some combination of changes forced by equatorial heating, topography, as well as other sources such as subtropical heating (Levine and Boos 2016, manuscript submitted to *J. Climate*) and land–sea thermal contrast (Shaw 2014). It remains an open problem to understand how the zonally asymmetric hydrological cycle in the real world responds to climate change in the presence of all of these different forcings.

Acknowledgments. This research has been supported by NSF Grant AGS-1019211. The idealized GCM simulations for this study were performed on ETH Zürich's EULER computing cluster. We thank Michael Byrne, Xavier Levine, Timothy Cronin, and an anonymous reviewer for useful comments and discussion during the development of this manuscript.

REFERENCES

- Betts, A. K., 1998: Climate-convection feedbacks: Some further issues. *Climatic Change*, **39**, 35–38, doi:10.1023/A:1005323805826.
- Boer, G. J., 1982: Diagnostic equations in isobaric coordinates. *Mon. Wea. Rev.*, **110**, 1801–1820, doi:10.1175/1520-0493(1982)110<1801:DEIIC>2.0.CO;2.
- Bony, S., G. Bellon, D. Klocke, S. Sherwood, S. Fermepein, and S. Denvil, 2013: Robust direct effect of carbon dioxide on tropical circulation and regional precipitation. *Nat. Geosci.*, **6**, 447–451, doi:10.1038/ngeo1799.
- Bordoni, S., 2007: On the role of eddies in monsoonal circulations: Observations and theory. Ph.D. thesis, University of California, Los Angeles, 195 pp.
- , and T. Schneider, 2008: Monsoons as eddy-mediated regime transitions of the tropical overturning circulation. *Nat. Geosci.*, **1**, 515–519, doi:10.1038/ngeo248.
- Brandefelt, J., and H. Körnich, 2008: Northern Hemisphere stationary waves in future climate projections. *J. Climate*, **21**, 6341–6353, doi:10.1175/2008JCLI2373.1.
- Broccoli, A., and S. Manabe, 1992: The effects of orography on mid-latitude Northern Hemisphere dry climates. *J. Climate*, **5**, 1181–1201, doi:10.1175/1520-0442(1992)005<1181:TEOOOM>2.0.CO;2.
- Byrne, M. P., and P. A. O’Gorman, 2013: Link between land-ocean warming contrast and surface relative humidities in simulations with coupled climate models. *Geophys. Res. Lett.*, **40**, 5223–5227, doi:10.1002/grl.50971.
- , and —, 2015: The response of precipitation minus evapotranspiration to climate warming: Why the “wet-get-wetter, dry-get-drier” scaling does not hold over land. *J. Climate*, **28**, 8078–8092, doi:10.1175/JCLI-D-15-0369.1.
- Chadwick, R., I. Boutle, and G. Martin, 2013: Spatial patterns of precipitation change in CMIP5: Why the rich do not get richer in the tropics. *J. Climate*, **26**, 3803–3822, doi:10.1175/JCLI-D-12-00543.1.
- Chen, J., and S. Bordoni, 2014: Orographic effects of the Tibetan Plateau on the East Asian summer monsoon: An energetic perspective. *J. Climate*, **27**, 3052–3072, doi:10.1175/JCLI-D-13-00479.1.
- Chou, C., and J. D. Neelin, 2004: Mechanisms of global warming impacts on regional tropical precipitation. *J. Climate*, **17**, 2688–2701, doi:10.1175/1520-0442(2004)017<2688:MOGWIO>2.0.CO;2.
- Frierson, D. M., 2007: The dynamics of idealized convection schemes and their effect on the zonally averaged tropical circulation. *J. Atmos. Sci.*, **64**, 1959–1976, doi:10.1175/JAS3935.1.
- , I. M. Held, and P. Zurita-Gotor, 2006: A gray-radiation aquaplanet moist GCM. Part I: Static stability and eddy scale. *J. Atmos. Sci.*, **63**, 2548–2566, doi:10.1175/JAS3753.1.
- Greve, P., B. Orlowsky, B. Mueller, J. Sheffield, M. Reichstein, and S. I. Seneviratne, 2014: Global assessment of trends in wetting and drying over land. *Nat. Geosci.*, **7**, 716–721, doi:10.1038/ngeo2247.
- Held, I. M., 1983: Stationary and quasi-stationary eddies in the extratropical troposphere: Theory. *Large-Scale Dynamical Processes in the Atmosphere*, B. Hoskins, Ed., Academic Press, 127–168.
- , and M. Ting, 1990: Orographic versus thermal forcing of stationary waves: The importance of the mean low-level wind. *J. Atmos. Sci.*, **47**, 495–500, doi:10.1175/1520-0469(1990)047<0495:OVTFO>2.0.CO;2.
- , and B. J. Soden, 2000: Water vapor feedback and global warming. *Annu. Rev. Energy Environ.*, **25**, 441–475, doi:10.1146/annurev.energy.25.1.441.
- , and —, 2006: Robust responses of the hydrological cycle to global warming. *J. Climate*, **19**, 5686–5699, doi:10.1175/JCLI3990.1.
- , M. Ting, and H. Wang, 2002: Northern winter stationary waves: Theory and modeling. *J. Climate*, **15**, 2125–2144, doi:10.1175/1520-0442(2002)015<2125:NWSWTA>2.0.CO;2.
- Hoskins, B. J., and D. J. Karoly, 1981: The steady linear response of a spherical atmosphere to thermal and orographic forcing. *J. Atmos. Sci.*, **38**, 1179–1196, doi:10.1175/1520-0469(1981)038<1179:TSLROA>2.0.CO;2.

- Knutson, T. R., and S. Manabe, 1995: Time-mean response over the tropical Pacific to increased CO₂ in a coupled ocean-atmosphere model. *J. Climate*, **8**, 2181–2199, doi:10.1175/1520-0442(1995)008<2181:TMROTT>2.0.CO;2.
- Levine, X. J., and T. Schneider, 2011: Response of the Hadley circulation to climate change in an aquaplanet GCM coupled to a simple representation of ocean heat transport. *J. Atmos. Sci.*, **68**, 769–783, doi:10.1175/2010JAS3553.1.
- Ma, J., S.-P. Xie, and Y. Kosaka, 2012: Mechanisms for tropical tropospheric circulation change in response to global warming. *J. Climate*, **25**, 2979–2994, doi:10.1175/JCLI-D-11-00048.1.
- Merlis, T. M., and T. Schneider, 2011: Changes in zonal surface temperature gradients and Walker circulations in a wide range of climates. *J. Climate*, **24**, 4757–4768, doi:10.1175/2011JCLI4042.1.
- Mitchell, J. F., C. Wilson, and W. Cunnington, 1987: On CO₂ climate sensitivity and model dependence of results. *Quart. J. Roy. Meteor. Soc.*, **113**, 293–322, doi:10.1256/smsqj.47516.
- Molnar, P., W. R. Boos, and D. S. Battisti, 2010: Orographic controls on climate and paleoclimate of Asia: Thermal and mechanical roles for the Tibetan Plateau. *Annu. Rev. Earth Planet. Sci.*, **38**, 77–102, doi:10.1146/annurev-earth-040809-152456.
- Newman, M., G. N. Kiladis, K. M. Weickmann, F. M. Ralph, and P. D. Sardeshmukh, 2012: Relative contributions of synoptic and low-frequency eddies to time-mean atmospheric moisture transport, including the role of atmospheric rivers. *J. Climate*, **25**, 7341–7361, doi:10.1175/JCLI-D-11-00665.1.
- O’Gorman, P. A., and T. Schneider, 2008: The hydrological cycle over a wide range of climates simulated with an idealized GCM. *J. Climate*, **21**, 3815–3832, doi:10.1175/2007JCLI2065.1.
- Rodwell, M. J., and B. J. Hoskins, 1996: Monsoons and the dynamics of deserts. *Quart. J. Roy. Meteor. Soc.*, **122**, 1385–1404, doi:10.1002/qj.49712253408.
- , and —, 2001: Subtropical anticyclones and summer monsoons. *J. Climate*, **14**, 3192–3211, doi:10.1175/1520-0442(2001)014<3192:SAASM>2.0.CO;2.
- Sardeshmukh, P. D., and B. J. Hoskins, 1988: The generation of global rotational flow by steady idealized tropical divergence. *J. Atmos. Sci.*, **45**, 1228–1251, doi:10.1175/1520-0469(1988)045<1228:TGOGRF>2.0.CO;2.
- Schneider, T., P. A. O’Gorman, and X. J. Levine, 2010: Water vapor and the dynamics of climate changes. *Rev. Geophys.*, **48**, RG3001, doi:10.1029/2009RG000302.
- Seager, R., and Coauthors, 2007: Model projections of an imminent transition to a more arid climate in southwestern North America. *Science*, **316**, 1181–1184, doi:10.1126/science.1139601.
- , N. Naik, and G. A. Vecchi, 2010: Thermodynamic and dynamic mechanisms for large-scale changes in the hydrological cycle in response to global warming. *J. Climate*, **23**, 4651–4668, doi:10.1175/2010JCLI3655.1.
- , H. Liu, N. Henderson, I. Simpson, C. Kelley, T. Shaw, Y. Kushnir, and M. Ting, 2014a: Causes of increasing aridification of the Mediterranean region in response to rising greenhouse gases. *J. Climate*, **27**, 4655–4676, doi:10.1175/JCLI-D-13-00446.1.
- , and Coauthors, 2014b: Dynamical and thermodynamical causes of large-scale changes in the hydrological cycle over North America in response to global warming. *J. Climate*, **27**, 7921–7948, doi:10.1175/JCLI-D-14-00153.1.
- Shaw, T. A., 2014: On the role of planetary-scale waves in the abrupt seasonal transition of the Northern Hemisphere general circulation. *J. Atmos. Sci.*, **71**, 1724–1746, doi:10.1175/JAS-D-13-0137.1.
- Shi, X., and D. R. Durran, 2014: The response of orographic precipitation over idealized midlatitude mountains due to global increases in CO₂. *J. Climate*, **27**, 3938–3956, doi:10.1175/JCLI-D-13-00460.1.
- Simpson, I. R., T. A. Shaw, and R. Seager, 2014: A diagnosis of the seasonally and longitudinally varying midlatitude circulation response to global warming. *J. Atmos. Sci.*, **71**, 2489–2515, doi:10.1175/JAS-D-13-0325.1.
- , R. Seager, M. Ting, and T. A. Shaw, 2016: Causes of change in Northern Hemisphere winter meridional winds and regional hydroclimate. *Nat. Climate Change*, **6**, 65–70, doi:10.1038/nclimate2783.
- Stephenson, D. B., and I. M. Held, 1993: GCM response of northern winter stationary waves and storm tracks to increasing amounts of carbon dioxide. *J. Climate*, **6**, 1859–1870, doi:10.1175/1520-0442(1993)006<1859:GRONWS>2.0.CO;2.
- Takahashi, K., and D. S. Battisti, 2007: Processes controlling the mean tropical Pacific precipitation pattern. Part II: The SPCZ and the southeast Pacific dry zone. *J. Climate*, **20**, 5696–5706, doi:10.1175/2007JCLI1656.1.
- Vecchi, G. A., and B. J. Soden, 2007: Global warming and the weakening of the tropical circulation. *J. Climate*, **20**, 4316–4340, doi:10.1175/JCLI4258.1.
- , —, A. T. Wittenberg, I. M. Held, A. Leetmaa, and M. J. Harrison, 2006: Weakening of tropical Pacific atmospheric circulation due to anthropogenic forcing. *Nature*, **441**, 73–76, doi:10.1038/nature04744.
- Voigt, A., and T. A. Shaw, 2015: Circulation response to warming shaped by radiative changes of clouds and water vapour. *Nat. Geosci.*, **8**, 102–106, doi:10.1038/ngeo2345.
- Wills, R. C., 2016: Stationary eddies and zonal variations of the global hydrological cycle in a changing climate. Ph.D. thesis, California Institute of Technology, 177 pp.
- , and T. Schneider, 2015: Stationary eddies and the zonal asymmetry of net precipitation and ocean freshwater forcing. *J. Climate*, **28**, 5115–5133, doi:10.1175/JCLI-D-14-00573.1.
- Wu, Y., M. Ting, R. Seager, H.-P. Huang, and M. A. Cane, 2011: Changes in storm tracks and energy transports in a warmer climate simulated by the GFDL CM2.1 model. *Climate Dyn.*, **37**, 53–72, doi:10.1007/s00382-010-0776-4.
- Xie, S.-P., C. Deser, G. A. Vecchi, J. Ma, H. Teng, and A. T. Wittenberg, 2010: Global warming pattern formation: Sea surface temperature and rainfall. *J. Climate*, **23**, 966–986, doi:10.1175/2009JCLI3329.1.